공 학 박 사 학 위 논 문

Development and Application of Classification Method for Electrochemical Oxidant Generating Electrodes

전기화학적 산화제 생성 전극의 분류법 개발 및 응용

2018년 8월

서울대학교 대학원

화학생물공학부

김 지 예

Abstract

Development and Application of Classification Method for Electrochemical Oxidant Generating Electrodes

Jiye Kim

School of Chemical and Biological Engineering

The Graduates School

Seoul National University

Electrochemical oxidants generation is widely used process for advanced oxidation process, wastewater treatment, chlor-alkali process, or polymerization. The oxidants such as chlorine (Cl_2), hydroxyl radical ($^{\bullet}OH$), peroxodisulfate (PDS), ozone (O_3), and hydrogen peroxide (H_2O_2) can be generated depends on the electrode materials and electrolysis conditions. Dimensionally stable anode (DSA®), boron doped diamond (BDD), and Sb-SnO_2 electrodes are widely used, also self-doped TiO_2 nanotube array (self-doped NTA; blue TNA and black TNA) and Bi-TiO_2/Ta-IrO_2 were recently

developed. According to the oxidants generating pathways, electrodes were classified as active and inactive electrode, which has limitations for differentiation of surface adsorbed $^{\bullet}OH$ and free $^{\bullet}OH$ and for classification of recently developed electrodes. Also, the mechanisms for oxidants generation along with the types of $^{\bullet}OH$ have not been proposed for the $^{\bullet}OH$ involving oxidants generation such as PDS which is the limitation for further development of electrodes. The development of novel electrodes with high performance is required by considering the oxidants generating pathways.

The objective of this study is the development of the electrode classification method for electrochemical oxidant generation by using the two types of $^{\bullet}OH$ scavengers (*t*-butanol and methanol) which have the different scavenging properties for surface adsorbed $^{\bullet}OH$ and free $^{\bullet}OH$. and its application to investigation of the precursor for PDS generation and to development of high performance chlorine generating electrode.

As major results, firstly, quantitative classification method for oxidant generating electrodes was developed. Ten electrodes were classified into active (A), inactive-surface adsorbed ($I_{\cdot OH,s}$), and inactive-free ($I_{\cdot OH,f}$). Also, those electrodes were quantitatively expressed according to the oxidants generating pathways as $\{R_A, R_{\cdot OH,s}, R_{\cdot OH,f}\}$ such as $RuO_2\{0.93, 0.07, 0\}$ and blue TNA{0.04, 0.17, 0.79} for the better understanding of oxidants generating properties of electrodes.

Secondly, the •OH species (surface adsorbed or free) was investigated to figure out the key precursor for PDS generation. PDS generation showed linear relationship with free •OH concentration measured by chlorine, which means that the free •OH is the key precursor for PDS generation. Also, blue TNA was reported for superior PDS generation with cost-effective material, which was comparable with that of BDD. The PDS generating efficiency on blue TNA and BDD were 46% and 41%, respectively. High PDS generation on blue TNA was due to the free •OH generation on blue TNA.

Thirdly, RuO_2 coated blue TNA was developed for superior chlorine generating electrode. Blue TNA-RuO_2 (96%) showed the higher chlorine generation efficiency than that of blue TNA (74%) and RuO_2 (82%), while the energy consumption for blue TNA-RuO_2 (3.2 Wh g^{-1}) was comparable to RuO_2 (3.3 Wh g^{-1}) and much lower than that of blue TNA (6.2 Wh g^{-1}). The reason for high performance on blue TNA-RuO_2 was the synergetic effect of direct and indirect pathways for chlorine generation.

The results of this study can improve the understanding of oxidants generating pathways, especially by using the novel classification method, and can contribute to the development of novel electrodes for highly efficient oxidants generation.

Keywords: Electrode classification, electrochemical oxidants generation, surface adsorbed hydroxyl radical, free hydroxyl radical, hydroxyl radical

scavenger, chlorine generation, peroxodisulfate generation, blue TiO_2 nanotube array.

Student Number: 2012-23976

Table of contents

List of Figures

List of Tables

1. Introduction

1.1. Backgrounds

The electrochemical oxidants generation is the process for generating oxidants from aqueous solutions by applying electric potential to the electrodes (Comninellis et al. 2008, Cañizares et al. 2009, Jeong et al. 2009, Sirés et al. 2014). Basically hydrogen and oxygen are generated on cathode and anode, respectively, from the water electrolysis. Also, various oxidants such as chlorine (Cl_2), hydroxyl radicals ($^{\bullet}OH$), persulfate ($S_2O_8^{2-}$, SO_5^{-}), ozone (O_3), or hydrogen peroxide (H_2O_2) are generated on the anode along with the oxygen during the electrolysis (Cañizares et al. 2009). Those oxidants are used for water treatment and industrial fields, such as degradation of toxic organic pollutants, disinfection, chlor-alkali industry, or polymerization (Comninellis 1994, Trasatti 2000, Iniesta et al. 2001, Cañizares et al. 2004, Jeong et al. 2009, Farhat et al. 2015). Furthermore, because of its feasibility, electrochemical oxidation process has been applied as the decentralized water treatment system in the low-infrastructure area to provide the safe drinking water by on-site water disinfection (Choi et al. 2013, Choi et al. 2013, Le Luu et al. 2014).

Recently, electrochemical water treatment process is getting interested in because it is environmentally sound, and safe technology compared with

conventional oxidation process which has to convey the toxic compounds to the water treatment site. The electrochemical system has advantages compare to the conventional oxidation process that the short life-time radical species is generated as intermediate compounds and those are effective oxidants with high oxidation power than other oxidants (Comninellis et al. 2008, Cañizares et al. 2009, Sirés et al. 2014).

There are the various electrode materials used for the oxidants generation. Dimensionally stable anode (DSA), boron doped diamond (BDD), self-doped TiO_2, Sb-SnO_2, Pt, or PbO_2 are widely used as an anode for electrochemical oxidants generation (Trasatti 1984, Marselli et al. 2003, Cao et al. 2013, Kim et al. 2014, Kim et al. 2015). Those electrodes are good for oxidants generation and pollutants degradation, but most of electrodes uses the precious metals such as Ir, Ru, or Pt. And in case of BDD, it has the complicated fabrication method such as chemical vapor deposition (CVD), and PbO_2 has a limitation for application because of its toxicity. Also, to improve efficiency, stability and feasibility of electrodes, novel electrodes were developed by varying fabrication method, coating metal oxide or composition of several metals (Yang et al. 2014, Cho et al. 2015). The choice of electrode material is important because the types of oxidants, generating efficiency, and the generating mechanisms is varied depends on the electrode materials. To improve the understandings of mechanism and oxidants

generating efficiency of electrode materials, three researches are further required.

Firstly, development of electrode classification is required considering the oxidants generating pathways. Until now, electrodes are classified as active and inactive electrode according to the oxidants generating mechanism (Comninellis 1994). DSA, including IrO_2 and RuO_2, is classified as active electrode while Sb-SnO_2, PbO_2, and BDD are classified as inactive electrode. The conventional active/inactive classification method provides the insight to understanding of electrode properties and facilitates the development of novel electrodes. However, the different oxidation properties of organic compounds were observed in between the inactive electrodes (Sb-SnO_2, PbO_2, and BDD) because of the generated $^{\bullet}OH$ species such as surface adsorbed or free $^{\bullet}OH$, which required the further researches for improving classification method by differentiating the $^{\bullet}OH$ species (Zhu et al. 2008).

Secondly, clarifying the intermediates for PDS generation is required to facilitate the development of efficient electrode. $^{\bullet}OH$ is known as the major precursor for PDS generation (Davis et al. 2014). However, the types of $^{\bullet}OH$ (surface adsorbed or free $^{\bullet}OH$) are not clearly defined, which would be the barrier for development of PDS generating electrode. Also, until now, BDD electrode is thoroughly investigated for PDS generation. Although BDD showed the high efficiency for PDS generation, the development of cost

effective electrode materials are required because of the expensive fabrication method of BDD electrode.

Thirdly, development of chlorine generating electrode with cost-effective materials are required. In the electrochemical chlorine generation process, DSA is widely used as anode material. However, because of the high cost of Ir or Ru, the reduction of material cost is the key concern in chlorine generation industries. Recently developed TiO_2 based electrodes showed the chlorine generation with cost effective material, while it had low efficiency compared to the DSA electrode (Kim et al. 2014) so that the improvement of chlorine generation of TiO_2 electrode is required.

1.2. Objectives

The objective of this study is the development of the classification method for electrochemical oxidant generating electrodes and its application to investigating the precursor for peroxodisulfate generation and to development of highly efficient chlorine generating electrode.

Firstly, a novel quantitative classification method for oxidant generating electrodes was developed. For this purpose, electrodes were classified according to the three pathways for oxidant generation: direct chlorine generation, surface adsorbed $^{\bullet}OH$, and free $^{\bullet}OH$ using two types of $^{\bullet}OH$ scavengers (*t*-butanol and methanol) to differentiate chlorine directly generated on the electrode surface from chlorine generated by the reaction of the chloride ions with $^{\bullet}OH$, which is surface adsorbed or free $^{\bullet}OH$. Additionally, all the electrodes were quantitatively defined to suggest new directions for developing innovative oxidant generating electrodes.

Secondly, the self-doped TiO_2 nanotube array electrodes (self-doped TNA electrodes) were examined for PDS generation which are cheap and efficient for generating a significant amount of $^{\bullet}OH$ and comparable to BDD electrodes. Also, the types of $^{\bullet}OH$ (surface adsorbed or free) were examined from the relationship between electrode classification method and PDS generation.

Thirdly, a novel electrode was fabricated by coating RuO_2 onto the blue TiO_2 nanotube array (blue TNA-RuO_2) to increase the chlorine generation of blue TNA using the direct and indirect pathways simultaneously on one electrode. The chlorine generation was studied on the blue TNA-RuO_2 electrode and compared to RuO_2 and blue TNA electrodes. Additionally, the direct and indirect oxidation pathways were investigated with a probe compound and scavenger for $^{\bullet}OH$.

2. Literature Review

2.1. Electrochemical Oxidants Generation

2.1.1. Electrochemical Chlorine Generation

2.1.1.1. Electrode for Chlorine Generation

Dimensionally Stable Anode (DSA®) is one of the important electrodes for oxidants generation. DSA has been widely used in the past 50 years especially for the chlorine generation in chlor-alkali process or electrochemical water treatment process (Trasatti 1984, Trasatti 1987). DSA is considered as the most important electrode because it is thermally and chemically stable, has low resistance, and has low overpotential for the oxygen and chlorine generation (Trasatti 1984, Trasatti 1987, Trasatti 2000, Over 2013, Kim et al. 2015).

Usually DSA electrode is fabricated by thermal decomposition of conductive metal oxide (ex. Rr or Ir) on the Ti substrate. To improve the efficiency, stability, or selectivity of DSA, many researches have been conducted such as nano-sized RuO_2 and IrO_2 electrode, or composite active material electrodes (Ferro et al. 2002, Jirkovský et al. 2006, Trieu et al. 2012, Cao et al. 2013).

2.1.1.2. Volcano Plot for Chlorine Generation

Over the several metal oxide electrodes, DSA electrode such as RuO_2 and IrO_2 is known as suitable material for the chlorine generation in terms of electrocatalytic activity. Volcano plot of electrochemical activity for chlorine generation has been suggested to figure out the reason for the superior chlorine generation on RuO_2 and IrO_2 (Trasatti 1984, Hansen et al. 2010, Zeradjanin et al. 2012). Figure 2-1 illustrates the oxygen evolution overpotential according to the enthalpy change when oxidation number increases on the metal oxide electrode with the water electrolysis. In case of metal oxide has low surface adsorption energy for the oxygen atom such as PbO_2, NiO_x, MnO_2, and PtO_2, oxidation of electrode is difficult because of its low adsorption ability, and adsorption of water on the electrode surface become a rate determining step which causes the low oxygen evolution property. On the other hand, Co_3O_4 and Fe_3O_4 electrode is easily oxidized but oxygen atom is too strongly adsorbed on the electrode surface to release the oxygen molecule which also causes the low oxygen evolution. That means, the appropriate adsorption energy leads the high oxygen evolution such as for the RuO_2 and IrO_2. Oxygen evolution is linearly related with the chlorine evolution so Figure 2-1 could be directly projected as an electrocatalytic activity of chlorine generation (Delahay et al. 1954, J. O'M 1956, Conway et al. 1964, Pankratiev 1982, Trasatti 1984, Cordfunke et al. 1988).

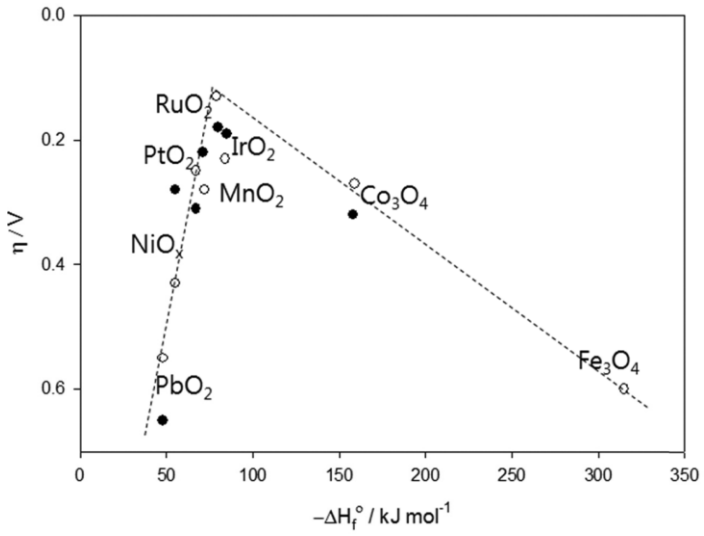

Figure 2-1. Electrocatalytic activity in O_2 evolution at various oxide electrodes as a function of the enthalpy of the lower to higher oxide transition.

○ alkaline and ● acid solutions are indicated (Trasatti 1984).

As a direct evidence for the volcano plot of chlorine activity, Raman shift was chosen as descriptor for elucidating the chlorine generation overpotential (Figure 2-2) (Zeradjanin et al. 2012). From the research of A. R. Zeradjanin et. al., overpotential of chlorine generation exhibits the volcano plot with raman shift. The superior electrocatalytic activities of RuO_2 and IrO_2 are explained with the vibration energy of Ru-O or Ir-O, which is similar with that of Cl-O bonding (Zeradjanin et al. 2012).

Also, adsorption energy of O atom was chosen as descriptor to interpret the electrocatalytic activities of RuO_2 and IrO_2 by calculating the density functional theory. As shown in Figure 2-3, adsorption energy of Cl, OH, O onto the electrode surface and binding energy of $Cl\text{-}O_{ad}$, $O\text{-}O_{ad}$, $Cl\text{-}O_{2,ad}$ were calculated to figure out the stable phase of electrode during the adsorption of Cl, OH, O atoms (grey line in Figure 2-3). Also, the Sabatier volcanoes were calculated for the chlorine generation reaction involving ClO^c, $Cl(O^c)_2$ and Cl^c (black dotted in Figure 2-3). Two factors were combined and the volcano plot with O^c as descriptor was obtained (black line in Figure 2-3). RuO_2 is positioned on the peak of volcano plot, which explains the high electrocatalytic activity of RuO_2 (Hansen et al. 2010).

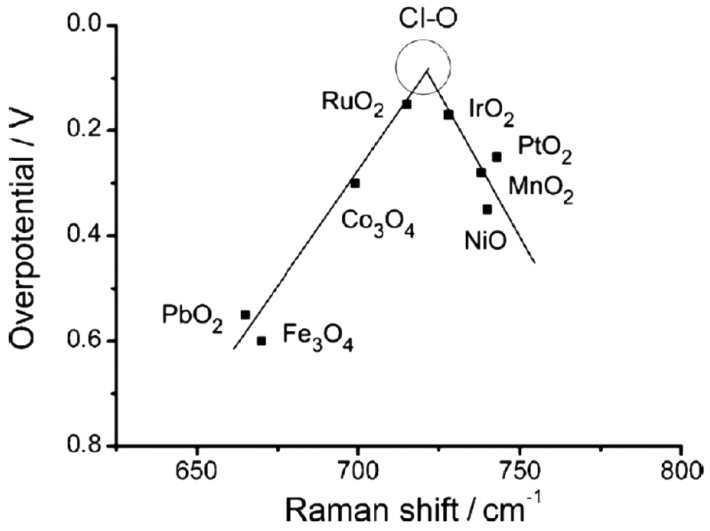

Figure 2-2. Overpotentials of the chlorine generation as a function of the characteristic Raman shift (Zeradjanin et al. 2012).

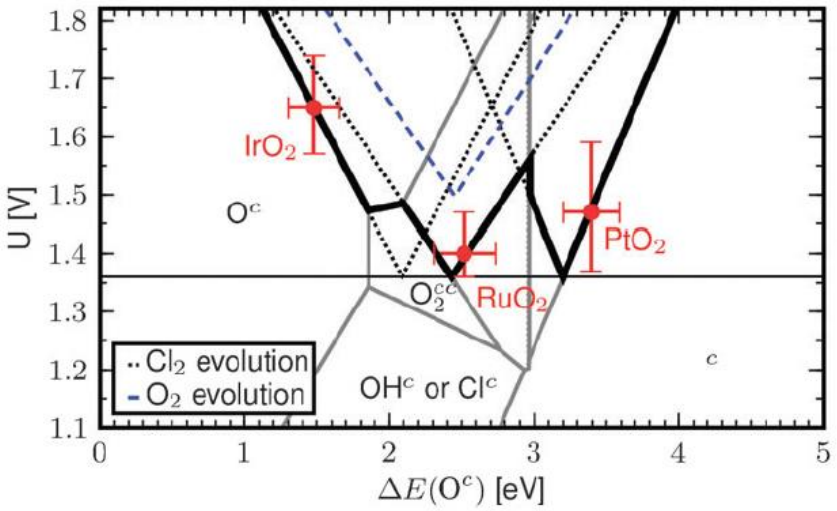

Figure 2-3. Volcano plot for chlorine generation with oxygen adsorption energy as descriptor.

Black dotted: Volcano plot for the reaction paths involving ClO^c, $Cl(O^c)_2$ and Cl^c (from left to right). Gray line: Most stable surface structure as function of potential and oxygen binding energy. Solid black line: Combined volcano plot taking into account the stability of the active sites. Dashed blue line: Volcano plot for oxygen evolution (Hansen et al. 2010).

2.1.1.3. Chlorine Generation Mechanism

Chlorine generation mechanism research was begun with revealing the rate determining step of chlorine generation reaction. Rate determining step was usually studied with the Tafel slope, which can be obtained from Butler-Volmer equation (Bard et al. 2001). Tafel slope by changing the electrode composition, electrolyte concentration, and in high overpotential range was measured to confirm the effect to the chlorine generation and to suggest the chlorine generation mechanism (Erenburg et al. 1975, Lodi et al. 1978, Losev et al. 1989). The Tafel slope of each chlorine generation reaction step was calculated by L. J. J. Janssen et al., at 1983, as shown in Figure 2-4 (Janssen et al. 1983). Tafel slope of the chloride ion adsorption on the electrode surface, the first step, was 118.4 mV/dec, and the second step, which adsorbed chloride release the electron, was 39.5 mV/dec. And the Tafel slope of the last step was 29.6 mV/dec, which is the diffusion out of chlorine. And these values were compared with the measured Tafel slope, which was 30 mV/dec, and the diffusion of chlorine from the electrode surface was verified as a rate determining step of chlorine generation reaction.

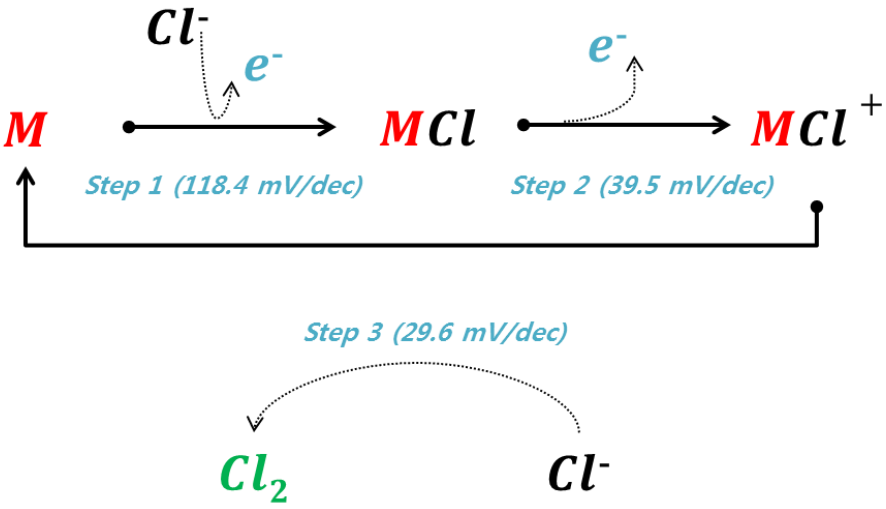

Figure 2-4. Tafel slope of each step in chlorine generation mechanism (Janssen et al. 1983).

As the experimental evidence, Figure 2-5 was examined by Faita and Fiori which shows the polarization curve according to the electrode materials. It illustrates that RuO_2 electrode has the similar Tafel slope with the Pt or Pt-Ir alloy electrode. Low Tafel slope (30-40 mV) which is similar with the previous studies means that the electrochemical-chemical mechanism is occurred, and that the diffusion of chlorine from the surface is rate determining step (Faita et al. 1972). Also, in the other research explained that the diffusion of Cl_2 control the chlorine generation rate because RuO_2 electrode is very active for the chlorine generation so that the adsorption of chloride and the electron transfer performed easily (Losev et al. 1989). These studies are widely accepted so that the diffusion of chlorine is the rate determining step of electrochemical chlorine generation on the DSA electrode (Chen et al. 2012).

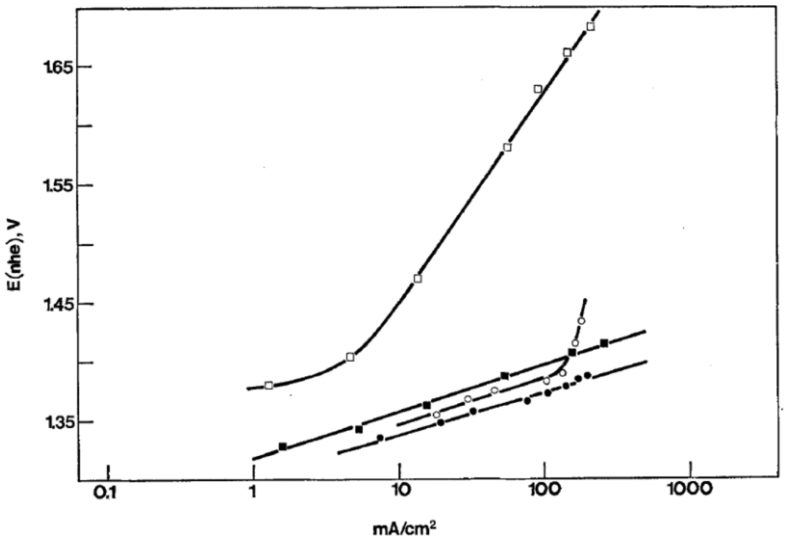

Figure 2-5. Polarization curves for various electrode materials.

□ graphite ■ RuO2 ○ Pt ● Pt-Ir(4%) (Faita et al. 1972).

Another important factor for studying the chlorine generation mechanism is identifying the reaction intermediate from Cl^- to Cl_2. The suggested reaction intermediates until now are Cl_{ad}, $(Cl_{ad})^+$, $(ClO_{ad})^-$, OCl_{ad}, $(M^{z+1})Cl_{ad}$, M(OH)Cl, M-OCl, $(O_2)_{ot}$-Cl and so on. In the early stage of mechanism research, only Cl_{ad} was considered as a reaction intermediate which is the adsorbed form of chloride ion on the electrode surface as shown in Reaction (2-1) and Reaction (2-2) (Erenburg et al. 1972).

$$Cl^- \rightleftarrows Cl_{ad} + e^- \qquad (2\text{-}1)$$

$$2Cl_{ad} \rightarrow Cl_2 \qquad (2\text{-}2a)$$

$$Cl_{ad} + Cl^- \rightarrow Cl_2 + e^- \qquad (2\text{-}2b)$$

However, $(Cl_{ad})^+$ was suggested as an another intermediate after the overall reaction order for the Cl^- was confirmed as 1 in 1975. So, the noble mechanism was suggested that the oxidation of Cl_{ad} to $(Cl_{ad})^+$ (Reaction (2-3)) and then the reaction of $(Cl_{ad})^+$ and Cl^- (Reaction (2-4)) to explain the reaction of Cl_{ad} and the Cl^- (Erenburg et al. 1975).

$$Cl^- \rightleftarrows Cl_{ad} + e^- \qquad (2\text{-}1)$$

$$Cl_{ad} \rightarrow (Cl_{ad})^+ + e^- \qquad (2\text{-}3)$$

$$(Cl_{ad})^+ + Cl^- \rightleftarrows Cl_2 \qquad (2\text{-}4)$$

However, the property of intermediate, $(Cl_{ad})^+$, was not mentioned but the form of intermediate could be $(HClO)_{ad}$ which is the form of oxidized electrode. Then, the $(ClO_{ad})^-$ was proposed as another intermediate with the X-ray photoelectron spectroscopy (XPS) results conducted by J. Augustynski et al., in 1978. With XPS, oxidation of electrode was observed which is caused by the oxygen, generated with water electrolysis, prior to the oxidation of chloride ion (Reaction (2-5)-(2-7)). However, it was elucidated that the actual form of chlorine is unpredictable whether it is trapped on the electrode surface, adsorbed on the surface, or get into the oxide layer (Augustynski et al. 1978).

$$RuO_2 + H_2O \rightarrow RuO_3 + 2H^+ + 2e \quad (2\text{-}5)$$

$$RuO_3 + Cl^- \rightarrow RuO_2(ClO_{ad})^- \quad (2\text{-}6)$$

$$(ClO_{ad})^- + Cl^-_{ad}\ (\text{or } Cl^-) + 2H^+ \rightarrow Cl_2 + H_2O \quad (2\text{-}7)$$

In another research conducted by L. K. Burke and J. F. O'Neill in 1979, oxygen surface site was proposed as the adsorption place for the Cl^- ion but that site is not participates to the redox reaction. That is, as shown in Reaction (2-8) and Reaction (2-9), the oxygen is firstly adsorbed on the electrode surface and chlorine adsorb on the oxygen to form OCl_{ad} which is the reaction intermediate for the chlorine generation reaction (Burke et al. 1979).

$$O_{ad} + Cl^- \rightarrow OCl_{ad} + e^- \quad (2\text{-}8)$$

$$OCl_{ad} + Cl^- \rightarrow O_{ad} + Cl_2 + e^- \quad (2\text{-}9)$$

Moreover, as elucidated in Reaction (2-10) to (2-12), review paper of L. I. Krishtalik in 1981 suggested the $(M^{Z+1})Cl_{ad}$ as an intermediate compound which chloride ion is adsorbed on the oxidized metallic surface (M^{Z+1}). And it means that the redox reaction of surface site is key factor for the chlorine generation as Reaction (2-10) (Krishtalik 1981).

$$(M^{z}) \rightleftarrows (M^{z+1}) + e^{-} \qquad (2\text{-}10)$$

$$(M^{z+1}) + Cl^{-} \rightarrow (M^{z+1})Cl_{ad} + e^{-} \qquad (2\text{-}11)$$

$$(M^{z+1})Cl_{ad} + Cl^{-} \rightleftarrows (M^{z}) + Cl_2 \qquad (2\text{-}12)$$

In the later research also described the redox reaction of surface site as a one of steps in chlorine generation mechanisms and suggested the adsorbed OHCl as a reaction intermediate (Hepel et al. 1986, Fernández et al. 2002, Thomassen et al. 2006). Furthermore, H. A. Hansen et al. suggest the $Cl(O^{c})_2$, ClO^{c}, and Cl^{c} as an intermediate for chlorine generation on the RuO_2, IrO_2, and PtO_2, respectively (Figure 2-6 for RuO_2). They calculate the adsorption energy of Cl, OH, and O on the cus site of electrode surface using the density functional theory calculation, and suggest the intermediate compounds when the electrodes are at the most stable state during the chlorine generation (Hansen et al. 2010).

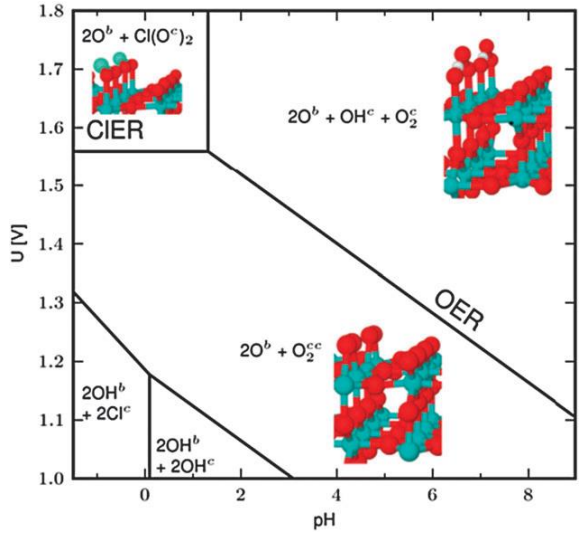

Figure 2-6. Surface phase diagram for RuO_2 (110) in equilibrium with Cl^-, H^+ and H_2O at 298.15 K.

The regions where we expect chlorine or oxygen evolution to become significant have been marked. ot and br denote on-top and bridge sites, respectively (Hansen et al. 2010).

2.1.2. Electrochemical Hydroxyl Radical Generation

In the electrochemical oxidation process, $^{\bullet}OH$ is generated from the water electrolysis on anode (Reaction (2-13)).

$$H_2O \rightarrow {}^{\bullet}OH + H^+ + e^- \qquad (2\text{-}13)$$

$^{\bullet}OH$ has high oxidation power compare to other oxidants ($E°[^{\bullet}OH/ H_2O] = 2.7$ V_{NHE}), it effectively degrade the organic compounds . Because of its high reactivity, it has short life time so that $^{\bullet}OH$ can be utilized in the on-site electrochemical oxidation process.

Several electrodes have been suggested for $^{\bullet}OH$ generation, such as boron doped diamond (BDD), Sb-SnO_2, or self-doped TiO_2 nanotube array (self-doped TNA). BDD has been gained great attention for the electrochemical oxidation process because of its high oxygen generation overpotential and stability, those properties facilitate the effective degradation of the organic compounds. However, BDD is fabricated by the chemical vapor deposition (CVD) method, which required the high temperature and pressure. High cost and complicate fabrication method limits the large scale production of BDD electrode so that the other $^{\bullet}OH$ generating electrodes were developed (Iniesta et al. 2001, Marselli et al. 2003, Cañizares et al. 2004, Panizza et al. 2005, Kapałka et al. 2008, Zhu et al. 2008).

Sb-SnO_2 was also known as $^{\bullet}OH$ generating electrode which has the high efficiency, easy fabrication method, and low toxicity. Also, several metal doped Sb-SnO_2 were suggested and Ni doped Sb-SnO_2 showed highest efficiency for $^{\bullet}OH$ generation. Sb-SnO_2 is usually fabricated by the thermal decomposition of Sb or Sn containing solution on the Ti substrate. This simple method facilitate the use of Sb-SnO_2 with large scale in industrial field. However, Sb-SnO_2 has low stability during the electrolysis, which require the further studies (Zhu et al. 2008, Cao et al. 2013, Yang et al. 2014).

Recently, self-doped TNAs was suggested as novel $^{\bullet}OH$ generating electrode. Although TiO_2 is insulator which cannot used for electrodes with low conductivity, self-doped TNA was suggested by increasing the electric conductivity from the cathodic polarization. Cathodic polarization reduce the Ti^{4+} to Ti^{3+}, and generate the oxygen vacancy. Increase of dopant level facilitate the use of TiO_2 as anode material. Also, self-doped TNA has nanotube structure which is the advantages for oxidants generation with high surface area (Figure 2-7). Depends on the doping level on TNA, the self-doped TNA is composed of blue and black TNAs. Both the black and blue TNAs have same nanotube structure with anatase phase, but the black TNA has the higher doping level than blue TNA. Both the blue and black TNAs are good for $^{\bullet}OH$ generation, while chlorine generation is superior on blue TNA (Kim et al. 2014, Kim et al. 2015, Kim et al. 2016, Kim et al. 2016).

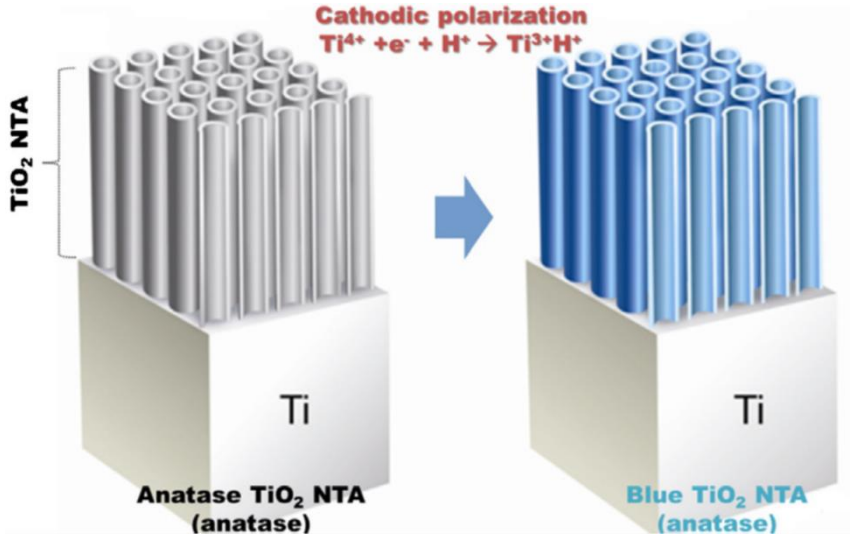

Figure 2-7. Blue TNA from the cathodic polarization (Kim et al. 2014).

2.1.3. Electrochemical Persulfate Generation

Peroxodisulfate (PDS, $S_2O_8^{2-}$), one of the strong oxidants with a high redox potential ($E°[S_2O_8^{2-}/HSO_4^-]$ = 2.12 V_{NHE}) (Michaud et al. 2000, Serrano et al. 2002, Bertsch-Frank et al. 2011, Davis et al. 2014), is frequently used as an initiator for the polymerization reaction. For example, PDS is used for olefin polymerization of polyacrylonitrile and for emulsion polymerization of vinyl chloride, styrene-butadiene, and acrylic esters (Bertsch-Frank et al. 2011). In addition, PDS is used to oxidize refractory organic compounds in wastewater and contaminated groundwater frequently by activation of sulfate radials ($SO_4^{-\bullet}$) ($E°[SO_4^{-\bullet}/SO_4^{2-}]$ = 2.5-3.1 V_{NHE}) (Neta et al. 1988, Wardman 1989, Farhat et al. 2015, Lee et al. 2015, Kim et al. 2016, Liu et al. 2016). Electrochemical PDS generation has the advantage in that PDS can be continuously generated on-site where PDS is required. In detail, PDS is electrochemically generated by the oxidation of HSO_4^- at a high potential. HSO_4^- and H_2SO_4 are known as the main species that react with $^{\bullet}OH$ for PDS generation (Palme 1920, Kolthoff et al. 1951). In a HSO_4^- electrolyte, there are two pathways for PDS generation. One is the reaction of $^{\bullet}OH$ with HSO_4^- (Reaction (2-14), (2-16)). The other is the direct one-electron oxidation of HSO_4^- (Reaction (2-15)). For the $^{\bullet}OH$ involved pathway, hydroxyl radicals ($^{\bullet}OH$) from water decomposition (Reaction (2-14)) react with hydrogen

sulfate (HSO_4^-) to generate $SO_4^{-\bullet}$ (Reaction (2-16)). Two molecules of $SO_4^{-\bullet}$ combine to generate PDS ($S_2O_8^{2-}$) (Reaction (2-17)) (Davis et al. 2014).

$$H_2O \rightarrow {}^{\bullet}OH + H^+ + e^- \quad (2\text{-}14)$$

$$HSO_4^- \rightarrow SO_4^{-\bullet} + H^+ + e^- \quad (2\text{-}15)$$

$$HSO_4^- + {}^{\bullet}OH \rightarrow H_2O + SO_4^{-\bullet} \quad (2\text{-}16)$$

$$2SO_4^{-\bullet} \rightarrow S_2O_8^{2-} \quad (2\text{-}17)$$

That is, the efficiency of the electrochemical PDS generation depends on the electrode materials. Because $^{\bullet}OH$ is the precursor for PDS, electrodes with a high oxygen evolution reaction (OER) overpotential can be used for PDS generation to minimize the oxygen evolution which is in competition with $^{\bullet}OH$ generation (Michaud et al. 2000, Serrano et al. 2002, Khamis et al. 2010). Initially, Pt electrodes were examined for electrochemical PDS generation, and later on, BDD electrodes became popular for electrochemical PDS generation. The current efficiency for PDS generation was reported as 20-47% on a BDD electrode in an acidic electrolyte at 20-25 ℃ (Smit et al. 1971, Michaud et al. 2000, Davis et al. 2014, Davis et al. 2014).

2.2. Classification of Oxidants Generating Electrodes

2.2.1. Classification of Active and Inactive Electrodes

Active/inactive classification have been proposed and generally discussed as classification method for oxidants generating electrodes (Trasatti 1984, Comninellis 1994). The active/inactive classification concept is shown in Figure 2-8 as suggested by the Comninellis group. The oxidant generating electrodes are divided into active and inactive electrodes, depending on the interaction between the electrode surface and the water molecules (Comninellis 1994).

From water electrolysis, $^{\bullet}OH$ adsorbed on the metal oxide (MO_x) surface becomes $MO_x(^{\bullet}OH)$. In the case of an active electrode, metal oxide (MO_x) is further oxidized to the higher oxidation state (MO_{x+1}). The DSA and Pt electrodes are known as active electrode. On the other hand, in the case of an inactive electrode, $MO_x(^{\bullet}OH)$ is transformed to the metal oxide (MO_x) without any change in the oxidation state. Because $^{\bullet}OH$ has a high potential for degrading organic compounds to CO_2, normally, an inactive electrode tends to have better decomposition of organic compounds compared to active electrodes (Comninellis et al. 2008). The BDD, PbO_2, and Sb-SnO_2 electrodes are known as inactive electrode.

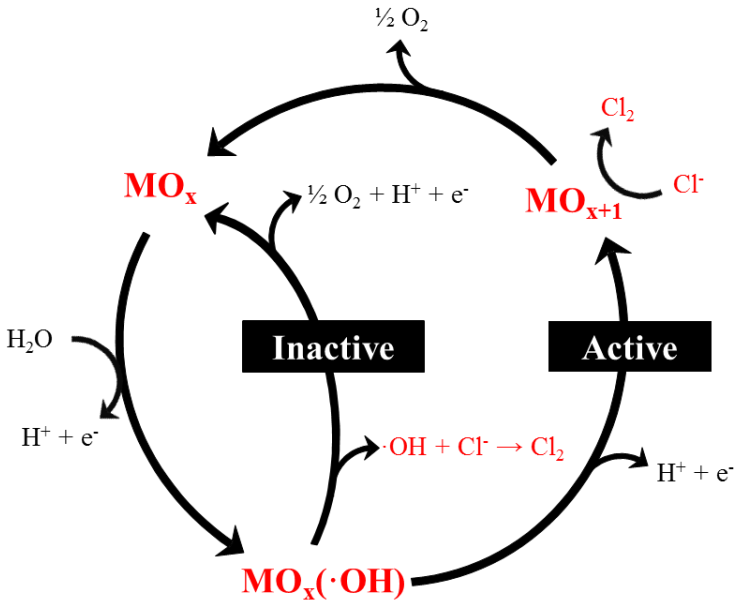

Figure 2-8. Existing classification method of active and inactive electrodes (Comninellis 1994).

2.2.2. Classification of Surface Adsorbed •OH and Free •OH

The BDD, PbO_2, and Sb-SnO_2 electrodes are known as inactive electrodes which generate the •OH. Because of the •OH generation, inactive electrodes are efficient for mineralization of organic compounds compare to the active electrodes. There were several researches to compare the organic oxidation in between the inactive electrodes. As shown in Figure 2-9, among the BDD, PbO_2, and Sb-SnO_2 electrodes, •OH generation on PbO_2 was highest and BDD was similar with that of Sb-SnO_2. Although the degradation of *p*-nitrophenol was similar in all three electrodes, the TOC removal, which means the mineralization of p-nitrophenol, was highest in BDD (Figure 2-10). In the literature, the reason for the excellent mineralization on BDD was discussed with its inert surface because BDD has no electrons in p or d orbitals so that the generated •OH on BDD is not adsorbed on the surface and diffused out as free radicals. While the surface adsorbed •OH is generated on the PbO_2 and Sb-SnO_2, there is limitation for the mineralization of organic compounds (Zhu et al. 2008).

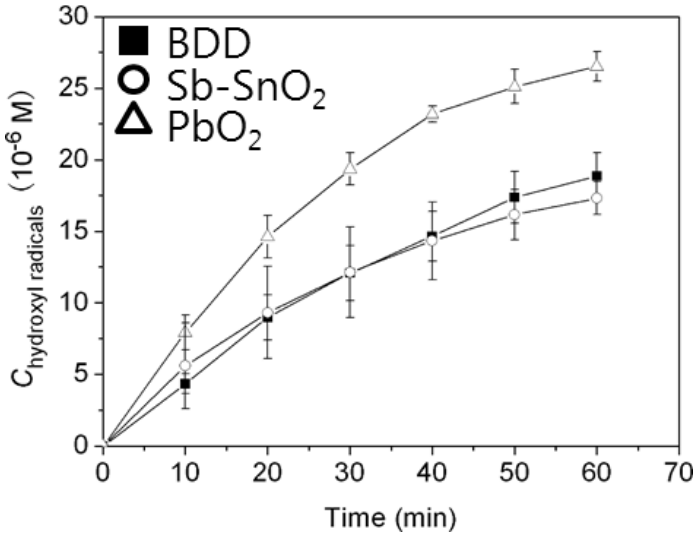

Figure 2-9. •OH generation on the BDD, Sb-SnO_2, and PbO_2 electrodes (Zhu et al. 2008).

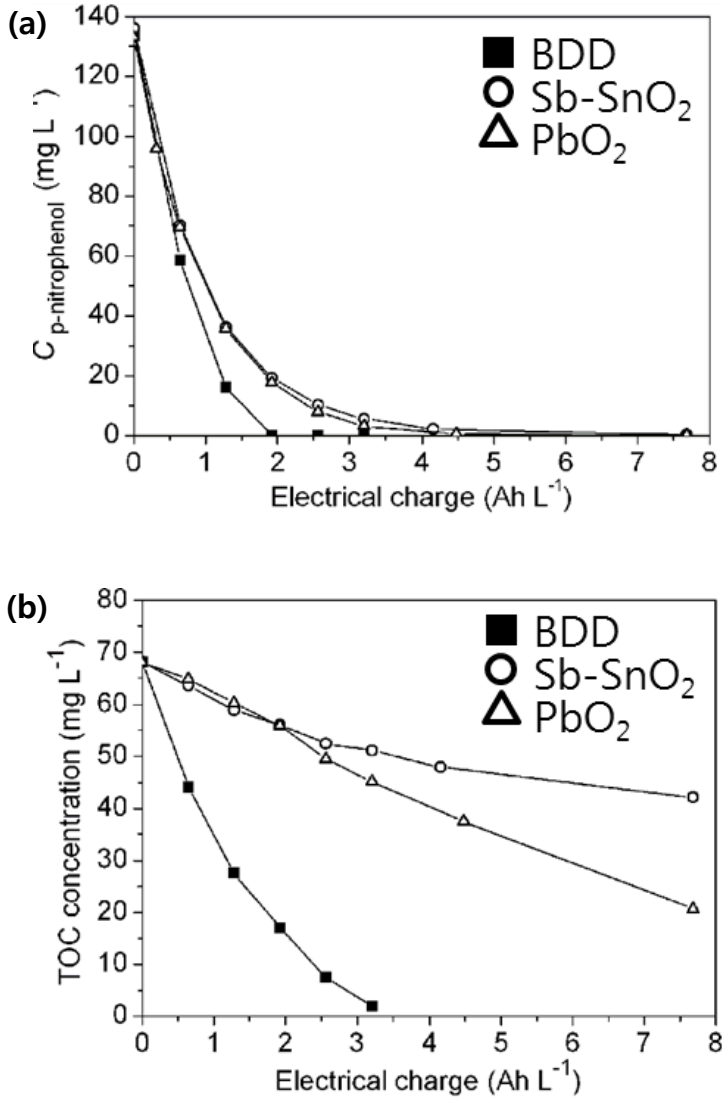

Figure 2-10. (a) *p*-nitrophenol degradation and (b) TOC removal on BDD, Sb-SnO_2, and PbO_2 electrodes (Zhu et al. 2008).

2.2.3. Classification Method for Surface Adsorbed •OH and Free •OH

As shown in Chapter 2.2.2, generated •OH species seems different according to the types of electrode as surface adsorbed •OH and free •OH. However, the method for differentiate those •OH species is not suggested in the electrochemical system.

On the other hand, in the photocatalytic oxidation process, the differentiation of surface adsorbed •OH and free •OH were performed using the *t*-butanol (*t*-BuOH) and methanol (MeOH) as •OH scavengers (Stafford et al. 1994, Sun et al. 1995, El-Morsi et al. 2000, Kim et al. 2002, Cho et al. 2005). The results revealed that the *t*-BuOH scavenges only free •OH while MeOH scavenges both the surface adsorbed and free •OH. This different scavenging effect in photocatalysis is firstly reported by Y. Sun and J. J. Pignatello in 1995 (Sun et al. 1995). They investigated the photocatalytic oxidation of 2,4-dichlorophenoxyacetic acid (2,4-D) with TiO_2, using the *t*-BuOH and MeOH as •OH scavengers. As shown in Figure 2-11, the results showed the no inhibition 2,4-D oxidation with *t*-BuOH and also *t*-BuOH showed low adsorption ability on the TiO_2 surface which is examined with Langmuir-Hinshelwood model. That is, the reaction occurred on the surface, so that the

lack of inhibition with *t*-BuOH is not due to the adsorption of *t*-BuOH on the surface, but due to the scavenging of free •OH.

Also, U. Stafford et al., S. Kim and W. Choi used the *t*-BuOH to scavenge free •OH for degradation of 4-chlorophenol, and $(CH_3)_nNH_{4-n}^+$ ($0 \leq n \leq 4$), respectively, and T. M. el-Morsi et al. used MeOH to scavenge both the surface adsorbed and free •OH for degradation of 1,10-Dichlorodecane (Figure 2-12) (Stafford et al. 1994, El-Morsi et al. 2000, Kim et al. 2002).

As shown in Figure 2-13, *t*-BuOH and MeOH were used as •OH scavengers and showed differences in *E. Coli* inactivation because *t*-BuOH scavenges only free •OH while MeOH scavenges both the surface adsorbed and free •OH (Cho et al. 2005).

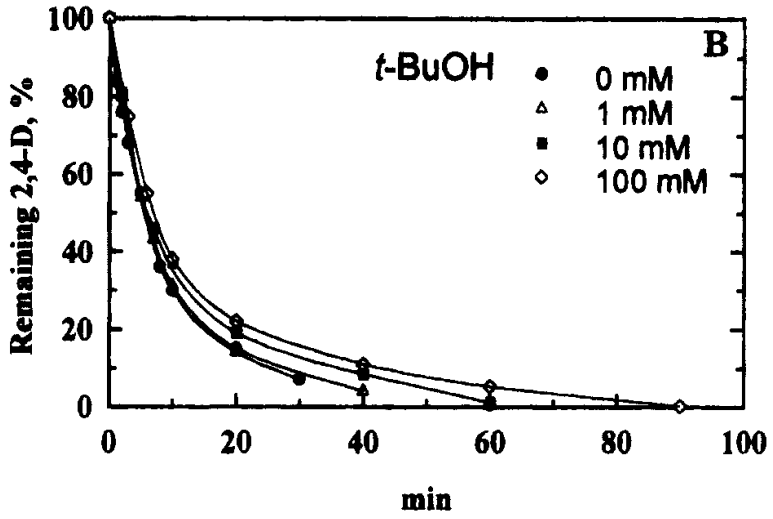

Figure 2-11. Effect of *t*-BuOH on degradation of 2,4-D (Sun et al. 1995).

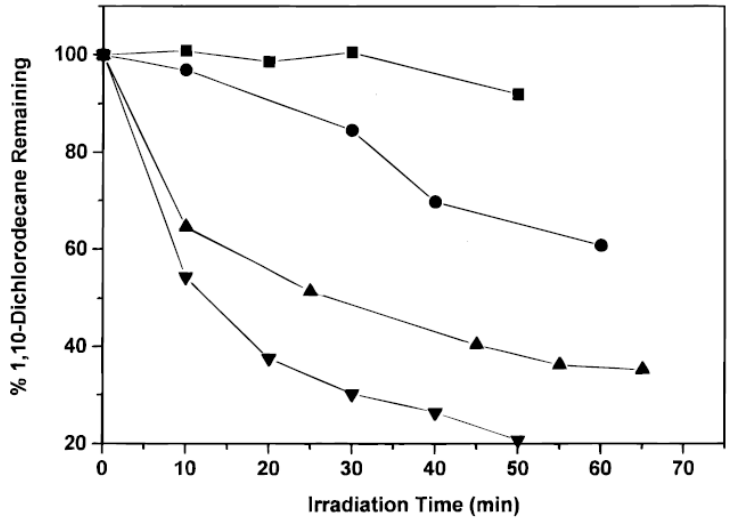

Figure 2-12. Effect of MeOH on the photodegradation of 1,10-dichlorodecane. MeOH concentrations: 0 mM (▼), 1 mM (▲), 10 mM (●), and 100 mM (■) (El-Morsi et al. 2000).

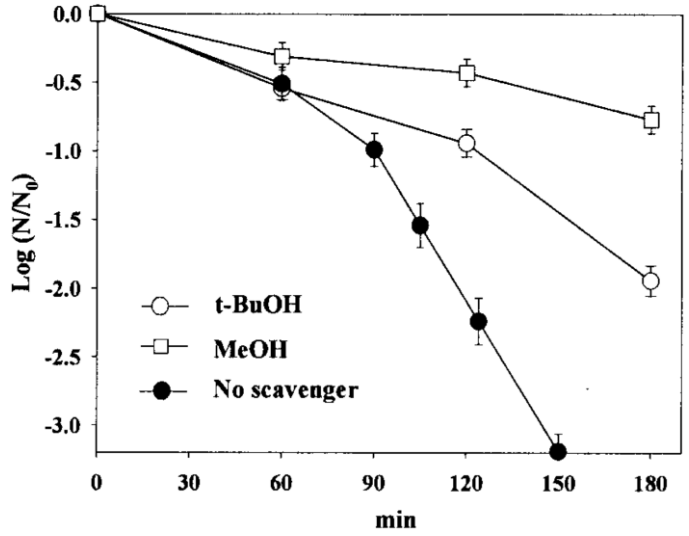

Figure 2-13. Inactivation of *E. Coli* in illuminated TiO_2 suspensions with $^{\bullet}OH$ scavengers (Cho et al. 2005).

3. Quantitative Classification Method for Oxidant Generating Electrodes with Respect to the Oxidant Generating Pathways

3.1. Introduction

This study developed a novel quantitative classification method for oxidant generating electrodes. Ten electrodes in total were used in this study including five active electrodes, RuO_2, IrO_2, Pt, Bi-TiO_2/Ta-IrO_2, and RuO_2-IrO_2, three inactive electrodes, Ni-Sb-SnO_2, Sb-SnO_2, and BDD, and two recently developed electrodes, blue and black TiO_2 nanotube arrays (blue and black TNAs) (Table 1). All the electrodes were classified according to the three pathways for oxidant generation: direct chlorine generation, surface adsorbed $^{\bullet}OH$, and free $^{\bullet}OH$. In case of $^{\bullet}OH$, because it is hard to measure the total amount of $^{\bullet}OH$ generation directly, an excess amount of chloride ions was used to determine the $^{\bullet}OH$ generation by measuring the chlorine formed as a result of the reaction of $^{\bullet}OH$ with chloride ions. Two types of $^{\bullet}OH$ scavengers (*t*-butanol and methanol) were used to differentiate chlorine directly generated on the electrode surface from chlorine generated by the reaction of the chloride ions with $^{\bullet}OH$, which is surface adsorbed or free $^{\bullet}OH$ (El-Morsi et al. 2000, Kim et al. 2002, Cho et al. 2005). Additionally, all the electrodes were

quantitatively defined to suggest new directions for developing innovative oxidant generating electrodes.

3.2. Materials and Methods

3.2.1. Preparation of the electrode materials

Ten anode materials in total were used in this study (Table 1). Four commercial electrodes (Pt, RuO_2-IrO_2, Bi-TiO_2/Ta-IrO_2, and BDD) and six fabricated electrodes (RuO_2, IrO_2, Sb-SnO_2, Ni-Sb-SnO_2, blue TNA, and black TNA) were used. Among the commercial electrodes, three (Pt, RuO_2-IrO_2, Bi-TiO_2/Ta-IrO_2) are known as active electrodes and BDD is known as inactive electrodes. The Pt electrode and RuO_2-IrO_2 electrode coated with Ru and Ir at a ratio of 50:50 mol% was obtained from Jinnys Co. and Elchemtech Co., respectively. Bi-TiO_2/Ta-IrO_2 and BDD were obtained from Nano-Pac Co. (Cho et al. 2015) and Condias GmbH, respectively. Among the six fabricated electrodes, two (RuO_2, IrO_2) are known as active electrodes, two (Sb-SnO_2, Ni-Sb-SnO_2) are known as inactive electrode, and two (blue TNA, black TNA) are unknown.

The fabrication methods of the six electrodes are described as follows. RuO_2, IrO_2, Sb-SnO_2, and Ni-Sb-SnO_2, and blue TNA and black TNA were fabricated with the thermal decomposition method (Le Luu et al. 2014), and anodization (Kim et al. 2014, Kim et al. 2015), respectively, as described in previous studies.

To fabricate the RuO_2 electrode, a Ti plate was polished with sand paper and etched in HCl at 80°C. After washing with deionized water, 1.7 μmol cm^-

^{2} of Ru precursor (0.2 M $RuCl_3$) was dropped on the pre-treated Ti plate. Then, the RuO_2 electrode was fabricated by annealing at 450℃ for 1 h. The IrO_2 electrode was fabricated with the same procedure as the RuO_2 electrode except for the precursor which was $IrCl_3$ (0.2 M). To fabricate the Sb-SnO_2 and Ni-Sb-SnO_2, a Ti plate was polished with sand paper, etched in HCl at 80 ℃, and washed with deionized water. Coating solution of $SnCl_4 \cdot 5H_2O$, $SbCl_3$, and $NiCl_2 \cdot 6H_2O$ (0.1 M, respectively) were prepared as Sn:Sb atomic ratio of 95:5, and Sn:Sb:Ni atomic ratio of 95:5:1. The pre-treated Ti plate were dipped into the coating solution and annealed at 450 ℃ for 5 min. The dipping and annealing procedures were repeated 10 times and further annealed at 450 ℃ for 1 h (Yang et al. 2014). To fabricate the blue TNA electrode, a Ti plate was anodized at 40 V for 5 h in an ethylene glycol solution which contained 0.2 wt% NH_4F and 2.5 wt% H_2O. The anodized Ti plate was annealed at 450℃ for 1 h in air. Then, cathodic polarization was performed in KH_2PO_4 solution (0.1 M) at 16.7 mA cm^{-2} for 90 s. To fabricate the Black TNA electrode, a Ti plate was anodized with the same method as the blue TNA and annealed at 200℃ for 1 h in air. Then, cathodic polarization was performed in the KH_2PO_4 solution (0.1 M) at 16.7 mA cm^{-2} for 90 s. It was further annealed at 450℃ for 1 h in N_2.

3.2.2. Electrolysis system and chemical analysis method

Oxidant generation by electrolysis was carried out in an undivided electrolytic cell (30 mL) with a constant current density (16.7 mA cm^{-2}) in NaCl electrolyte (0.1 M). Ten different electrode materials, as mentioned in Table 1, were used as the anode with a working geometric area of 1.5 cm^2 (1 cm x 1.5 cm), while the same size of platinum mesh was used as the cathode.

To figure out the effect of scavenger concentration, 0.02 to 0.5 M of t-BuOH and MeOH were used to measure the $^{\bullet}OH$ scavenging effect to chlorine generation on the RuO_2, Sb-SnO_2, and BDD electrodes with a constant current density (5, 16.7, and 50 mA cm^{-2}). Scavenging effect was expressed by the ratio of chlorine generation with scavenger and the chlorine generation without scavenger. To figure out the effect of current density to electrode classification, RuO_2, Sb-SnO_2, and BDD was representatively examined for electrode classification on the constant current density of 5, 16.7, and 50 mA cm^{-2}.

The concentration of active chlorine was determined as mg/L (as total Cl_2) at 530 nm with the N,N-diethyl-p-phenylenediamine (DPD) colorimetric method using a spectrophotometer (DR/2010, HACH Co., Loveland, USA) (APHA, 2005) (Association et al. 2005).

Two methods were used to assess the $^{\bullet}OH$ production. First, an excess amount (0.2 M) of *t*-butanol (*t*-BuOH) or methanol (MeOH), well-known $^{\bullet}OH$

scavengers, was introduced to differentiate chlorine directly generated on the electrode surface from chlorine generated by the reaction of $^{\bullet}OH$ with the chloride ions (El-Morsi et al. 2000, Kim et al. 2002, Cho et al. 2005). Second, *p*CBA, a well-known probe compound for $^{\bullet}OH$ was used to estimate the $^{\bullet}OH$ production. The initial concentration of *p*CBA was 300 μg/L in KH_2PO_4 electrolyte (0.1 M). The degradation of *p*CBA was analyzed by HPLC (YL9100, Younglin Co., Korea). A C18 reverse phase column (5 μm, 150 mm x 4.6 mm) was used, and the concentration of *p*CBA was detected at 230 nm with a UV detector. A solvent mixture of 35% acetonitrile / 65% water containing 40 mM phosphate buffer was used as the mobile phase (Elovitz et al. 1999).

3.2.3. Classification method of oxidants generating electrodes

Figure 3-1 shows the oxidant generating electrode classification method proposed in this study according to the three pathways for oxidant generation (Jeong et al. 2009, Rueffer et al. 2011). First, chlorine is generated directly on the electrode surface in the presence of excess chloride ions (Figure 3-1(a)). Second, $^{\bullet}$OH generated on the electrode surface was presumed to exists in two forms; surface adsorbed $^{\bullet}$OH and free $^{\bullet}$OH. This concept is slightly evolved from a previous study regarding the status of $^{\bullet}$OH adsorbed on the electrode surface shown in Figure 3-1 (El-Morsi et al. 2000, Kim et al. 2002, Cho et al. 2005). Then, the $^{\bullet}$OH, which is generated in two ways, reacts with the chloride ions to generate chlorine (Figure 3-1(b), (c)) (El-Morsi et al. 2000, Kim et al. 2002).

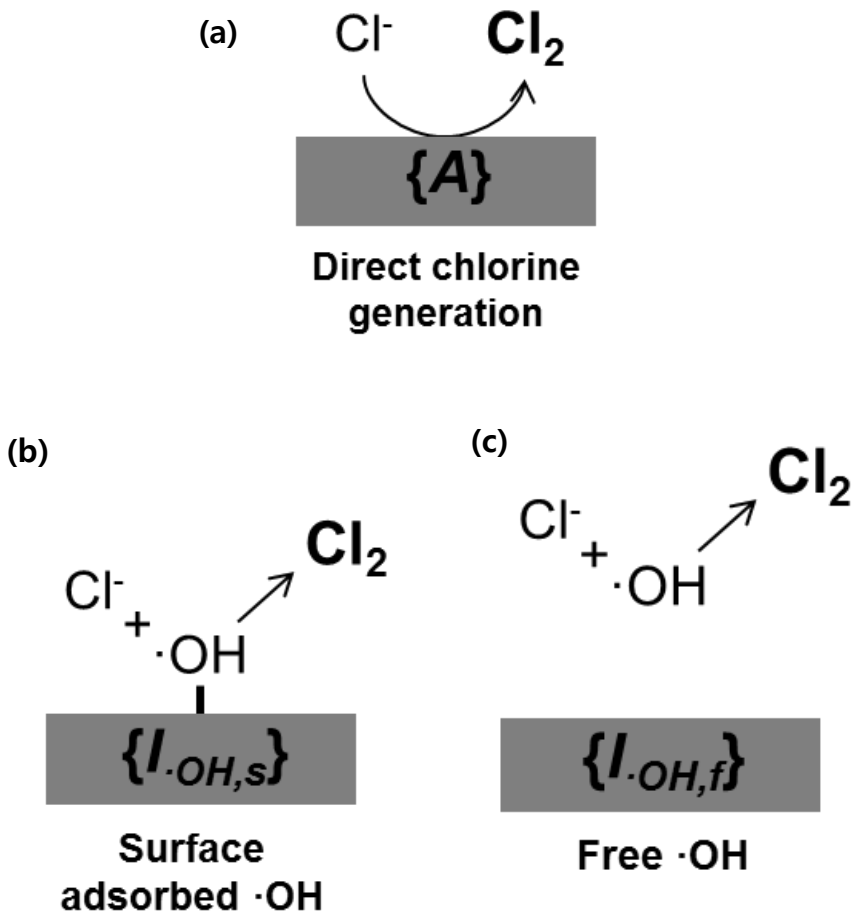

Figure 3-1. Classification of electrodes according to three pathways for oxidant generation.

(a) The pathway for chlorine generation through a direct surface reaction. (b) The pathway for surface adsorbed $^{\bullet}$OH generation. (c) The pathway for free $^{\bullet}$OH generation. Both the surface adsorbed & free $^{\bullet}$OH are presumed to generate chlorine as a result of the reaction of $^{\bullet}$OH with the chloride ions.

As shown in Figure 3-1(a)-(c), Active {A}, Inactive-Surface adsorbed {$I_{\cdot OH,s}$}, and Inactive-Free {$I_{\cdot OH,f}$} represent the electrodes which have a strong tendency for chlorine generation through the direct reaction, the reaction with the surface adsorbed $^{\bullet}$OH, and the free $^{\bullet}$OH, respectively. The Cl_2 concentration generated on each type of electrode is denoted as $Cl_{2,A}$, $Cl_{2,\cdot OH,s}$, and $Cl_{2,\cdot OH,f}$. Then, the total Cl_2 concentration ($Cl_{2,total}$) is defined as follows (Equation (3-1)).

$$Cl_{2,total} = Cl_{2,A} + Cl_{2,\cdot OH,s} + Cl_{2,\cdot OH,f} \quad (3\text{-}1)$$

The $^{\bullet}$OH scavenger was intentionally used to identify the directly generated chlorine and the chlorine by the reaction of $^{\bullet}$OH with the chloride ions. Two types of $^{\bullet}$OH scavenger were used to differentiate the surface adsorbed $^{\bullet}$OH from the free $^{\bullet}$OH. *t*-BuOH is known as a scavenger only for free $^{\bullet}$OH and not for the surface adsorbed $^{\bullet}$OH (Figure 3-2(a)) (Kim et al. 2002, Cho et al. 2005). On the other hand, MeOH can scavenge both the surface adsorbed $^{\bullet}$OH and free $^{\bullet}$OH (Figure 3-2(b)) (El-Morsi et al. 2000, Cho et al. 2005).

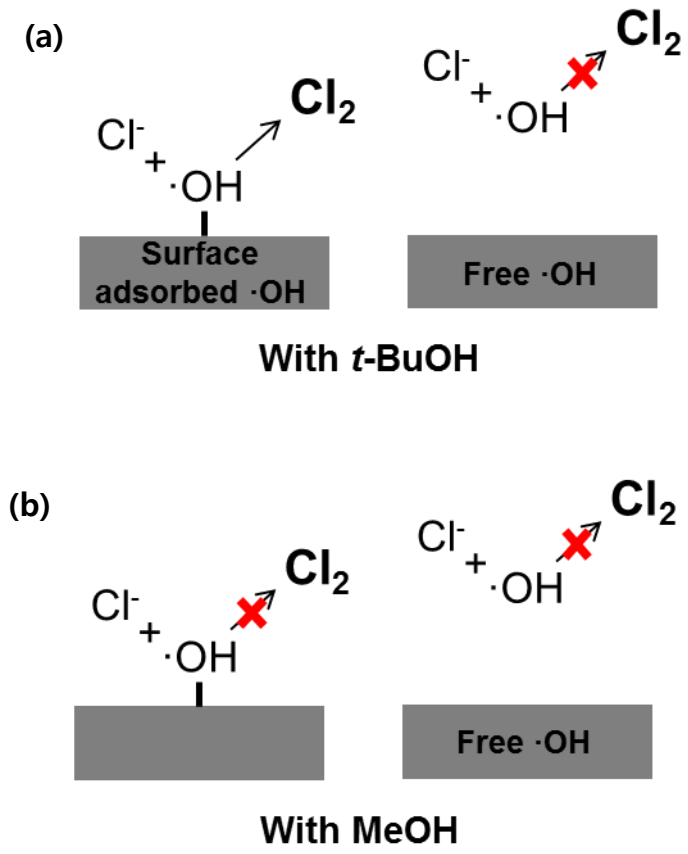

Figure 3-2. (a) Scavenging of the free •OH using *t*-BuOH. (b) Scavenging of both the surface adsorbed and free •OH using MeOH.

The Cl_2 measurement in the presence of *t*-BuOH and MeOH was denoted as $Cl_{2,t\text{-BuOH}}$ and $Cl_{2,\text{MeOH}}$, respectively. $Cl_{2,A}$, $Cl_{2,\cdot OH,s}$, and $Cl_{2,\cdot OH,f}$ were expressed with $Cl_{2,t\text{-BuOH}}$ and $Cl_{2,\text{MeOH}}$ as follows (Equation (3-2) to (3-4)).

$$Cl_{2,A} = Cl_{2,\text{MeOH}} \quad (3\text{-}2)$$

$$Cl_{2,\cdot OH,s} = Cl_{2,t\text{-BuOH}} - Cl_{2,\text{MeOH}} \quad (3\text{-}3)$$

$$Cl_{2,\cdot OH,f} = Cl_{2,\text{total}} - Cl_{2,t\text{-BuOH}} \quad (3\text{-}4)$$

R_A, $R_{\cdot OH,s}$, and $R_{\cdot OH,f}$ are defined to express the fractional characteristics of the oxidant generation of each electrode, that is, the proportion of each oxidant out of the total oxidants generated (Equation (3-5) to (3-7)). Note that the sum of R_A, $R_{\cdot OH,s}$, and $R_{\cdot OH,f}$ becomes equal to one (Equation (3-8)).

$$R_A = \frac{Cl_{2,A}}{Cl_{2,\text{total}}} = \frac{Cl_{2,\text{MeOH}}}{Cl_{2,\text{total}}} \quad (3\text{-}5)$$

$$R_{\cdot OH,s} = \frac{Cl_{2,\cdot OH,s}}{Cl_{2,\text{total}}} = \frac{Cl_{2,t-\text{BuOH}} - Cl_{2,\text{MeOH}}}{Cl_{2,\text{total}}} \quad (3\text{-}6)$$

$$R_{\cdot OH,f} = \frac{Cl_{2,\cdot OH,l}}{Cl_{2,\text{total}}} = \frac{Cl_{2,\text{total}} - Cl_{2,t-\text{BuOH}}}{Cl_{2,\text{total}}} \quad (3\text{-}7)$$

$$R_A + R_{\cdot OH,s} + R_{\cdot OH,f} = 1 \quad (3\text{-}8)$$

If an electrode of interest belongs to one of the R_A, $R_{\cdot OH,s}$, and $R_{\cdot OH,f}$ with more than 0.75 (75%), its corresponding electrode is defined to belong to the $\{A\}$ electrode, $\{I_{\cdot OH,s}\}$ electrode, or $\{I_{\cdot OH,f}\}$ electrode, respectively. If it does not belong to any of the cases of R_A, $R_{\cdot OH,s}$, and $R_{\cdot OH,f}$ with 0.75 (75%) but the sum of the two is more than 75%, its corresponding electrode is designated as the $\{A\&I_{\cdot OH,s}\}$ electrode or $\{I_{\cdot OH,s}\&I_{\cdot OH,f}\}$ electrode. No $\{A\&I_{\cdot OH,l}\}$ electrodes were observed.

3.3. Results and Discussion

3.3.1. Effect of scavenger concentrations

Figure 3-3 to 3-5 shows the effect of concentrations of $^{\bullet}OH$ scavengers (*t*-BuOH and MeOH) to scavenging effect of chlorine generation on RuO_2 (Figure 3-3), Sb-SnO_2 (Figure 3-4), and BDD (Figure 3-5) electrodes, representatively, at different current density as (a) 5, (b) 16.7, and (c) 50 mA cm^{-2}. Scavenging effect (C/C_0) means the ratio of chlorine generation with and without scavengers. As shown in Figure 3-3, there was no difference in scavenging effect on RuO_2 electrode with the concentration and the types of scavengers in all current densities, which means that the $^{\bullet}OH$ did not affect to the chlorine generation on RuO_2. In case of Sb-SnO_2, scavenging effect increases by increasing the concentration of scavengers and scavenging effect remain unchanged over 0.2 M of scavengers as 20% and 60% for *t*-BuOH and MeOH, respectively (Figure 3-4). That is, the chlorine is partly generated from free $^{\bullet}OH$ and surface adsorbed $^{\bullet}OH$ on the Sb-SnO_2 electrode. Figure 3-5 shows the scavenging effect of chlorine generation on BDD electrode. As shown in Figure 3-5, scavenging effect was steadily increased according to the scavenger concentration on the BDD electrode in both the *t*-BuOH and MeOH. No chlorine generation was observed over 0.2 M of scavengers.

According to the results of Fiugre 3-3 to 3-5, 0.2 M of scavengers are excess amount for scavenging the $^{\bullet}OH$ in the chlorine generation conditions in RuO_2,

Sb-SnO_2 and BDD electrode, and the experiments in below was conducted in 0.2 M of *t*-BuOH or MeOH as excess amount of $^{\bullet}OH$ scavengers.

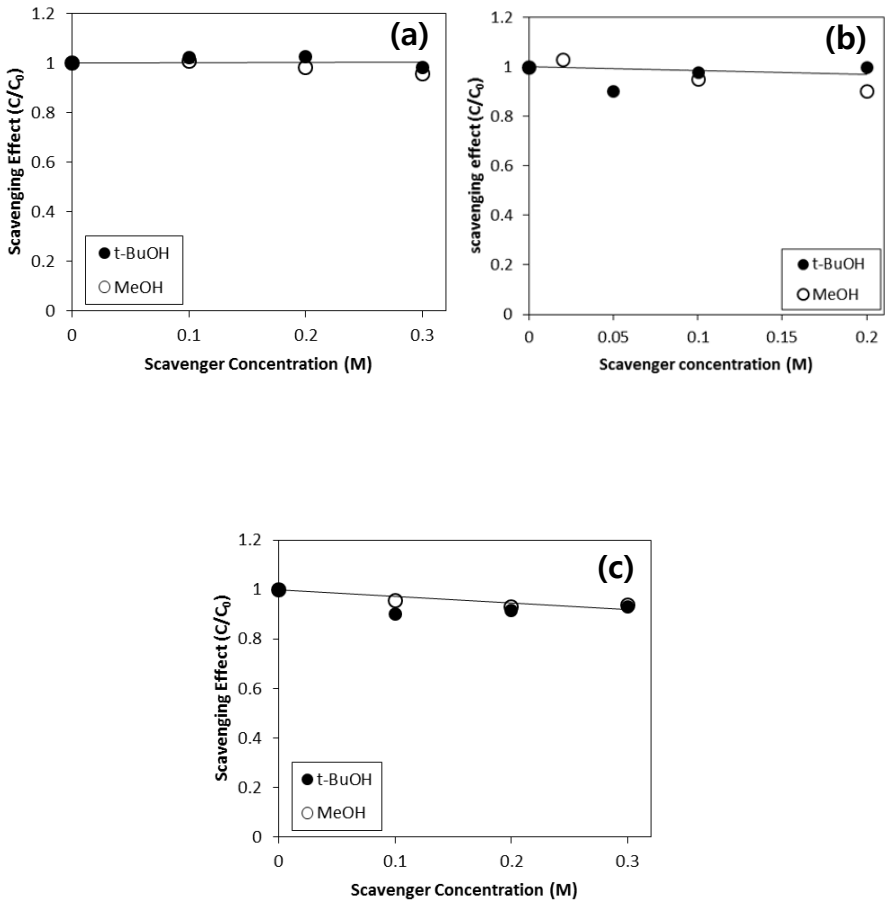

Figure 3-3. Effect of concentrations of •OH scavengers (*t*-BuOH and MeOH) to chlorine generation on RuO_2 electrode

at (a) 5 mA cm^{-2}, (b) 16.7 mA cm^{-2}, and (c) 50 mA cm^{-2}, representatively ($[NaCl]_0$ = 0.1 M, $[t\text{-BuOH}]_0$ = 0.02 to 0.3 M, $[MeOH]_0$ = 0.02 to 0.3 M, 7 min, pH 6.5, 25℃).

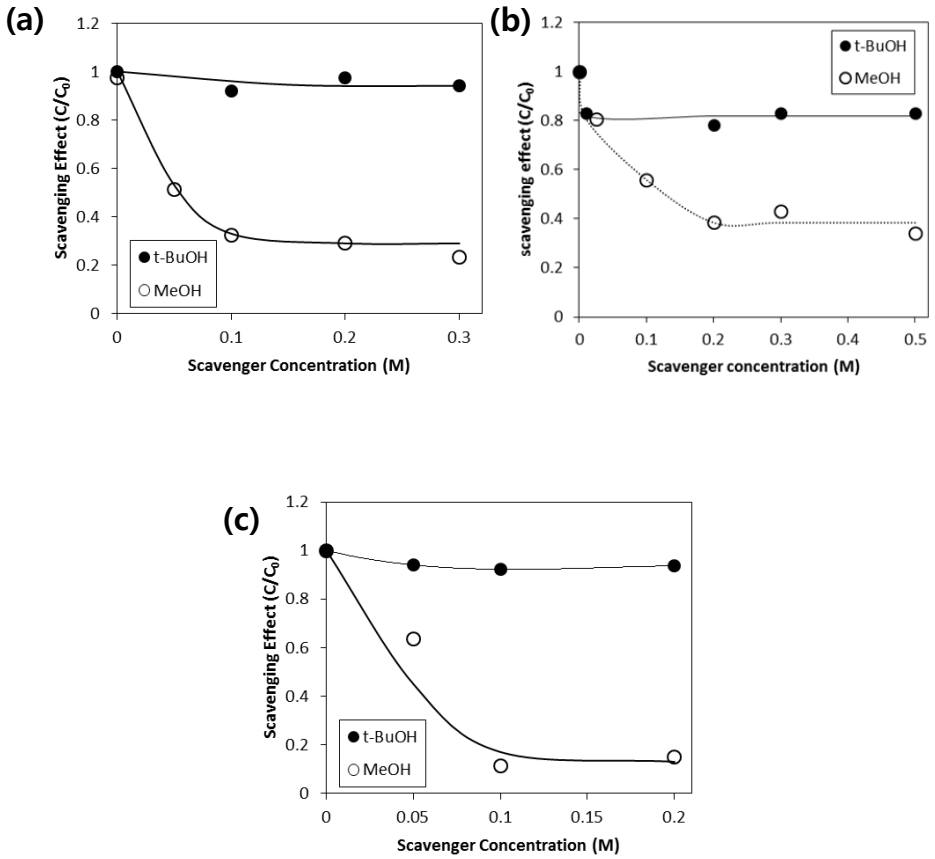

Figure 3-4. Effect of concentrations of •OH scavengers (*t*-BuOH and MeOH) to chlorine generation on Sb-SnO_2 electrode

at (a) 5 mA cm^{-2}, (b) 16.7 mA cm^{-2}, and (c) 50 mA cm^{-2}, representatively ($[NaCl]_0$ = 0.1 M, $[t\text{-BuOH}]_0$ = 0.02 to 0.5 M, $[MeOH]_0$ = 0.02 to 0.5 M, 7 min, pH 6.5, 25℃).

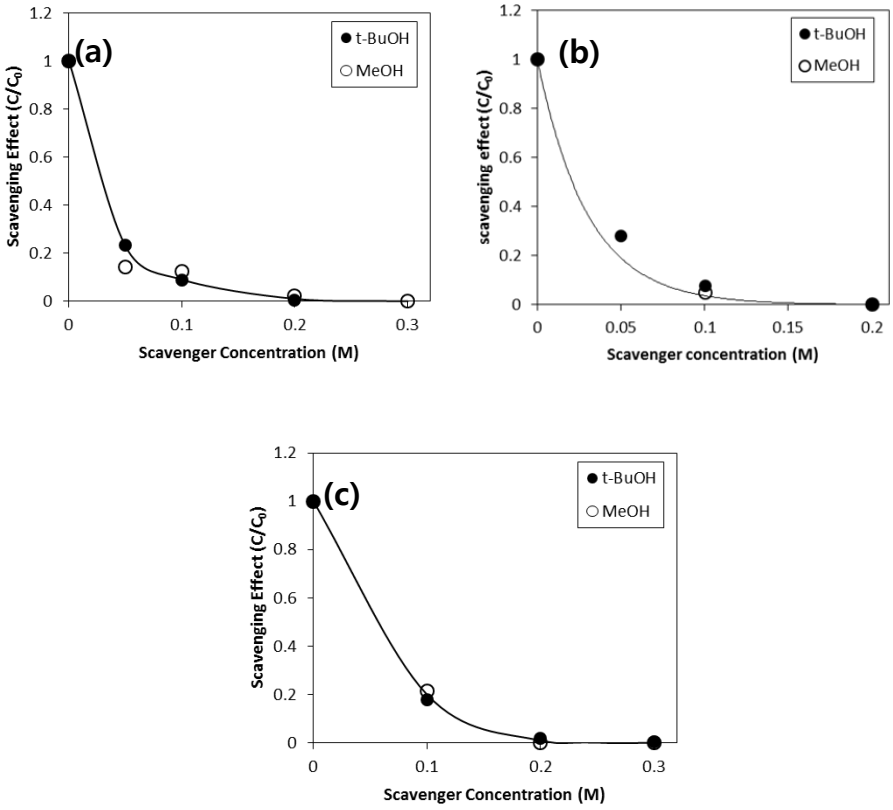

Figure 3-5. Effect of concentrations of •OH scavengers (*t*-BuOH and MeOH) to chlorine generation on BDD electrode

at (a) 5 mA cm^{-2}, (b) 16.7 mA cm^{-2}, and (c) 50 mA cm^{-2}, representatively ($[NaCl]_0$ = 0.1 M, $[t\text{-BuOH}]_0$ = 0.05 to 0.3 M, $[MeOH]_0$ = 0.05 to 0.3 M, 7 min, pH 6.5, 25℃).

3.3.2. Effect of current density

Figure 3-6 shows the chlorine generation with $^{\bullet}OH$ scavenger according to the current densities on (a) RuO_2, (b) Sb-SnO_2, and (c) BDD electrode. As shown in Figure 3-6(a), the chlorine generation was 35, 84, and 204 mg/L during 7 min electrolysis on RuO_2 with the current density as 5, 16.7, and 50 mA cm^{-2}, respectively. The chlorine generating current efficiency was 90% at 5 mA cm^{-2} of current density, which the side reaction was less than 10%. The current efficiency was 65% and 53% for 16.7 and 50 mA cm^{-2}, respectively, due to the significant side reaction such as oxygen generation. Note that there is not significant difference for chlorine generation when the *t*-BuOH and MeOH was used for $^{\bullet}OH$ scavengers.

As shown in Figure 3-6(b), the chlorine generation was 19, 42, and 102 mg/L during 7 min electrolysis on Sb-SnO_2 with the current density as 5, 16.7, and 50 mA cm^{-2}, respectively. The chlorine generating current efficiency was 48%, 33%, and 26% at 5, 16.7, and 50 mA cm^{-2}, respectively, due to the significant side reaction such as oxygen generation. The current efficiency was decreased by increasing the current density. Also, part of chlorine generation was inhibited when the *t*-BuOH was added as $^{\bullet}OH$ scavenger, and the scavenging was more significant for MeOH. The scavenging effect was consistent with the current densities.

As shown in Figure 3-6(c), the chlorine generation was 16, 36, and 112 mg/L during 7 min electrolysis on BDD with the current density as 5, 16.7, and 50 mA cm^{-2}, respectively. The chlorine generating current efficiency was 41%, 28%, and 29% at 5, 16.7, and 50 mA cm^{-2}, respectively, due to the significant side reaction such as oxygen generation. The current efficiency was decreased by increasing the current density and remain similar over 16.7 mA cm^{-2}. Also, almost all of chlorine generation was inhibited when the *t*-BuOH and MeOH was added as $^{\bullet}OH$ scavenger. The scavenging effect was consistent with the current densities.

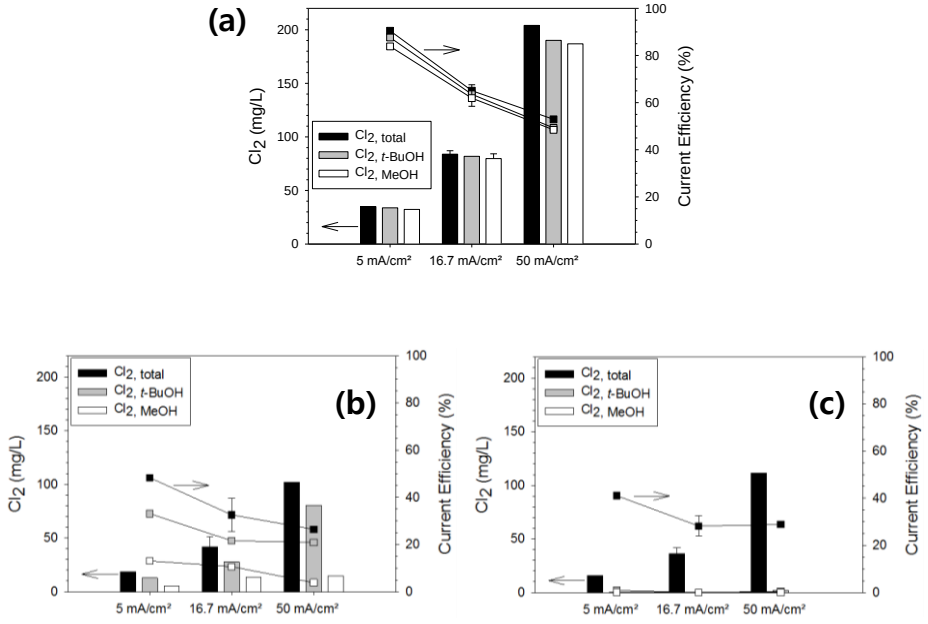

Figure 3-6. Chlorine generation with •OH scavenger according to the current densities on (a) RuO_2, (b) Sb-SnO_2, and (c) BDD electrode.

Bar graph indicates the generated chlorine concentration and line graph indicates the current efficiency for chlorine generation ($[NaCl]_0$ = 0.1 M; $[t\text{-}BuOH]_0$ = 0.1 M; $[MeOH]_0$ = 0.1 M; 7 min, 5, 16.7, and 50 mA cm^{-2}; pH 6.5; 25℃).

Figure 3-7 shows the fractional characteristics of the oxidant generation on the RuO_2, Sb-SnO_2 and BDD electrodes depending on the current densities. As shown in Figure 3-7, RuO_2 showed the negligible scavenging effect with t-BuOH and MeOH, which is classified as active electrode. In case of Sb-SnO_2, chlorine generation is partly inhibited with $^{\bullet}OH$ scavenger, that is, Sb-SnO_2 is classified as $I_{^{\bullet}OH,s}$ and $I_{^{\bullet}OH,f}$ electrode. BDD, which showed the effective scavenging with both the *t*-BuOH and MeOH, is classified as $I_{^{\bullet}OH,f}$ electrode. Note that the electrode classification is not significantly changed according to the current densities in all electrodes.

Table 3-1 shows the quantitative classification of electrodes according to the pathways for oxidant generation in different current densities. As shown in Table 3-1, the electrodes were quantitatively expressed based on the results of Figure 3-7. As mentioned above, the electrode classification is not significantly changed according to the current densities in all electrodes.

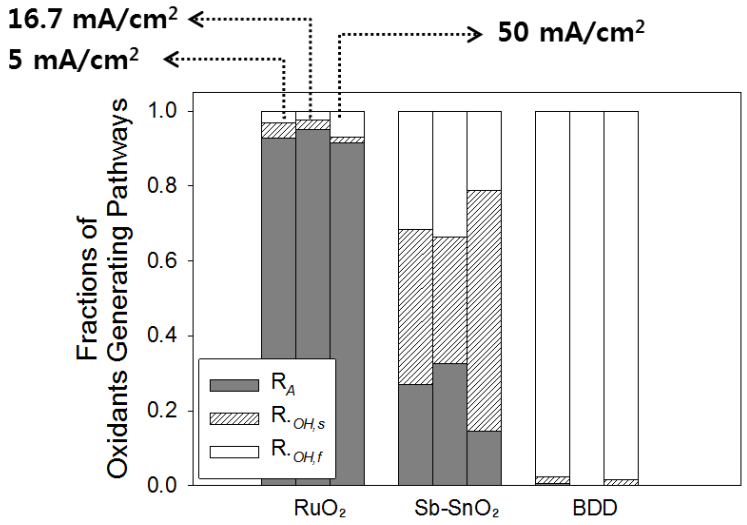

Figure 3-7. Fractional characteristics of the oxidant generation (R_A, $R_{\cdot OH,s}$, and $R_{\cdot OH,f}$) depending on the current densities.

R_A: Fraction of direct chlorine generation, $R_{\cdot OH,s}$: Fraction of surface adsorbed $^{\bullet}OH$ generation, and $R_{\cdot OH,f}$: Fraction of free $^{\bullet}OH$ generation ($[NaCl]_0$ = 0.1 M, $[t\text{-BuOH}]_0$ = 0.2 M, $[MeOH]_0$ = 0.2 M, 7 min, 5, 16.7, and 50 mA cm^{-2}, pH 6.5, 25℃).

	5 mA cm^{-2}	**16.7 mA cm^{-2}**	**50 mA cm^{-2}**
RuO_2	{0.93, 0.04, 0.03}	{0.95, 0.03, 0.02}	{0.92, 0.01, 0.07}
Sb-SnO_2	{0.27, 0.41, 0.32}	{0.33, 0.33, 0.34}	{0.15, 0.64, 0.21}
BDD	{0, 0.02, 0.98}	{0, 0, 1}	{0, 0.02, 0.98}

Table 3-1. Quantitative classification of electrodes according to the pathways for oxidant generation in different current densities.

3.3.3. Chlorine generation with and without $^{\bullet}$OH scavenger

Figure 3-8 shows the characteristics of the total (or partial) oxidant generation for the various electrode materials (RuO_2, IrO_2, Pt, Bi-TiO_2/Ta-IrO_2, RuO_2-IrO_2, Ni-Sb-SnO_2, Sb-SnO_2, black TNA, blue TNA, and BDD) measured with chlorine generation in the absence or presence of $^{\bullet}$OH scavengers (*t*-BuOH, MeOH).

As shown in Figure 3-8, the $Cl_{2,total}$ of the electrodes examined varied greatly from 30.0 to 102.5 mg/L under identical experimental conditions. For example, the RuO_2-IrO_2 electrode had the highest $Cl_{2,total}$ (102.5 mg/L), and the Black TNA had the lowest $Cl_{2,total}$ (30.0 mg/L). The DSA electrodes (such as RuO_2, IrO_2, and RuO_2-IrO_2) had a relatively high $Cl_{2,total}$, over 70 mg/L, compared with the other electrodes.

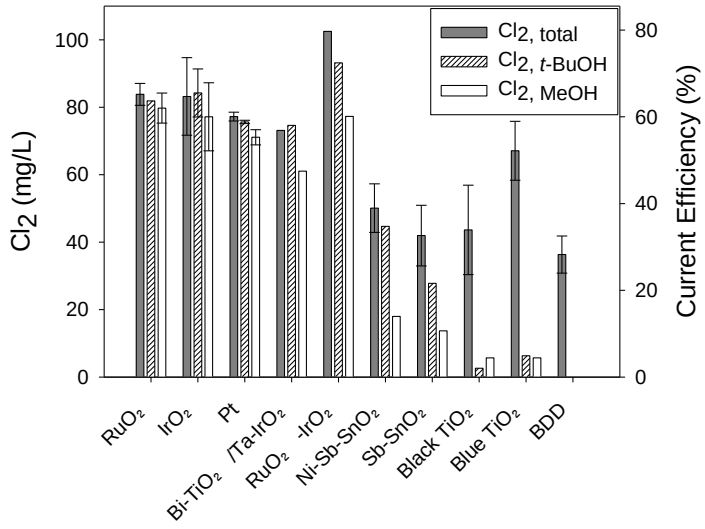

Figure 3-8. Characteristics of the total (or partial) oxidant generation and current efficiency on the various electrode materials measured with chlorine generation in the absence or presence of $^{\bullet}$OH scavengers (*t*-BuOH, MeOH). ($[NaCl]_0$ = 0.1 M, $[t\text{-BuOH}]_0$ = 0.2 M, $[MeOH]_0$ = 0.2 M, 7 min, 16.7 mA cm^{-2}, pH 6.5, 25℃).

Figure 3-9 shows the fractional characteristics of the oxidant generation ($R_{A,}$ $R_{\cdot OH,s}$, and $R_{\cdot OH,f}$) for the various electrode materials (RuO_2, IrO_2, Pt, Bi-TiO_2/Ta-IrO_2, RuO_2-IrO_2, Ni-Sb-SnO_2, Sb-SnO_2, black TNA, blue TNA, and BDD), depending on the generating pathway obtained with Equation (3-5) to (3-7).

Three significant observations can be addressed in Figure 3-8 and Figure 3-9. First, the reduction of chlorine generation appears to be small in these electrodes (RuO_2, IrO_2, Pt, Bi-TiO_2/Ta-IrO_2 and RuO_2-IrO_2) when *t*-BuOH and MeOH were used as $^{\bullet}OH$ scavengers, indicating the high fraction of $R_{A,}$ and these electrodes are classified as {*A*} electrode. Second, in the case of the Ni-Sb-SnO_2 and Sb-SnO_2 electrode, part of the chlorine was decreased with *t*-BuOH and almost all of the chlorine was suppressed with MeOH, indicating that significant portions of both $R_{\cdot OH,s}$ and $R_{\cdot OH,f}$ exist, and the electrode is classified as $\{I_{\cdot OH,s}\&I_{\cdot OH,f}\}$ electrode. Third, in the case of the black TNA, blue TNA and BDD electrode, almost all of the chlorine generation was suppressed with both the *t*-BuOH and MeOH, indicating the high fraction of $R_{\cdot OH,f}$, and this electrode is classified as $\{I_{\cdot OH,f}\}$.

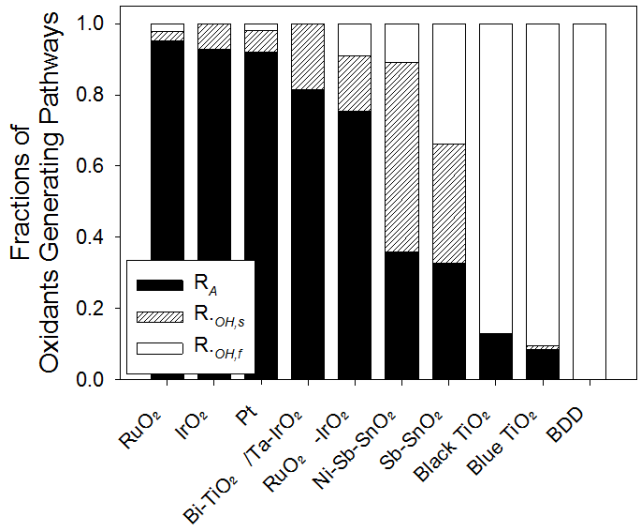

Figure 3-9. Fractional characteristics of the oxidant generation (R_A, $R_{\cdot OH,s}$, and $R_{\cdot OH,f}$), depending on its generating pathway.

R_A: Fraction of direct chlorine generation, $R_{\cdot OH,s}$: Fraction of surface adsorbed $^{\bullet}OH$ generation, and $R_{\cdot OH,f}$: Fraction of free $^{\bullet}OH$ generation ($[NaCl]_0$ = 0.1 M, $[t\text{-BuOH}]_0$ = 0.2 M, $[MeOH]_0$ = 0.2 M, 7 min, 16.7 mA cm^{-2}, pH 6.5, 25℃).

3.3.4. Relationship between the •OH concentration and Oxygen Evolution Reaction (OER) Overpotential with Electrode Classification

Figure 3-10 shows the relationship between the steady state •OH generation ($[^{\bullet}OH]_{ss}$) and the concentration of •OH generation measured as chlorine ($Cl_{2,\cdot OH,s} + Cl_{2,\cdot OH,f}$). *p*CBA was used as the •OH probe compound to obtain the $[^{\bullet}OH]_{ss}$, and $Cl_{2,\cdot OH,s} + Cl_{2,\cdot OH,f}$ of each electrode were calculated from Figure 3-8 and Equation (3-3) and (3-4).

As shown in Figure 3-10, in general, $Cl_{2,\cdot OH,s} + Cl_{2,\cdot OH,f}$ are proportional to $[^{\bullet}OH]_{ss}$, and the electrodes with the high $[^{\bullet}OH]_{ss}$ are closer to the inactive electrode as seen by the black TNA, blue TNA, and BDD. These observations support that the measurement of •OH through the reaction of •OH with chloride corresponds with the $[^{\bullet}OH]_{ss}$ measured by the •OH probe compound, indicating that this novel classification method is reliable to determine the concentration of •OH by measuring the chlorine concentration. Additionally, Figure 3-10 supports that the novel classification method corresponds with previous research which shows high •OH generation on the inactive electrode (Comninellis 1994, Marselli et al. 2003). In the case of the Ni-Sb-SnO_2 electrode, its result is not observed in Figure 3-10 because this electrode has $[^{\bullet}OH]_{ss}$ more than 10^{-13} M with 0.45 mM of $Cl_{2,\cdot OH,s} + Cl_{2,\cdot OH,f}$. A good

explanation is not available at present, and further studies are required to explain the results of $[^{\bullet}OH]_{ss}$ in the Ni-Sb-SnO_2 electrode.

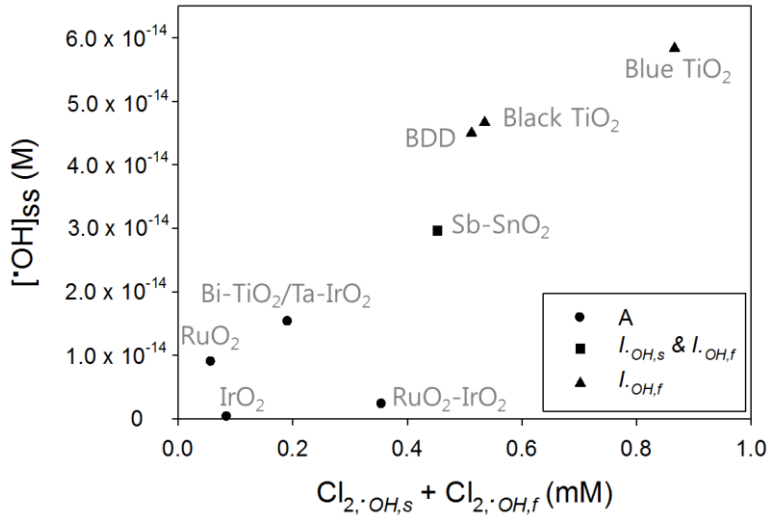

Figure 3-10. Relationship between steady state •OH generation ($[^{\bullet}OH]_{ss}$) measured by the •OH probe compound (*p*CBA) and •OH generation measured as chlorine generation ($Cl_{2,\cdot OH,s} + Cl_{2,\cdot OH,f}$).

$Cl_{2,\cdot OH,s}$: Concentration of surface adsorbed •OH measured by chlorine; $Cl_{2,\cdot OH,f}$: Concentration of free ·OH measured by chlorine ($[KH_2PO_4]_0$ = 0.1 M, $[p\text{CBA}]_0$ = 1.92 μM, 30 min for $[^{\bullet}OH]_{ss}$ measurement, $[NaCl]_0$ = 0.1 M, 7 min for Cl_2 measurement, 16.7 mA cm^{-2}, pH 7.4, 25℃).

Figure 3-11 shows the relationship between oxygen evolution reaction (OER) overpotential and the fractional characteristics of electrodes calculated from the chlorine generation. As shown in Figure 3-11(a), OER overpotential and R_A showed the inverse linear relationship with R^2 = 0.88. That is, the electrodes with high R_A exhibit the tendency for low OER overpotential while the OER oeverpotential showed less relationship with $R_{\cdot OH,s}$ or $R_{\cdot OH,f}$ (Figure 3-11(b), (c)). The OER overpotential is known to linearly relate to chlorine generation. Moreover, Figure 3-11 reveals that the OER overpotential is related to the direct chlorine generation (R_A), more specifically.

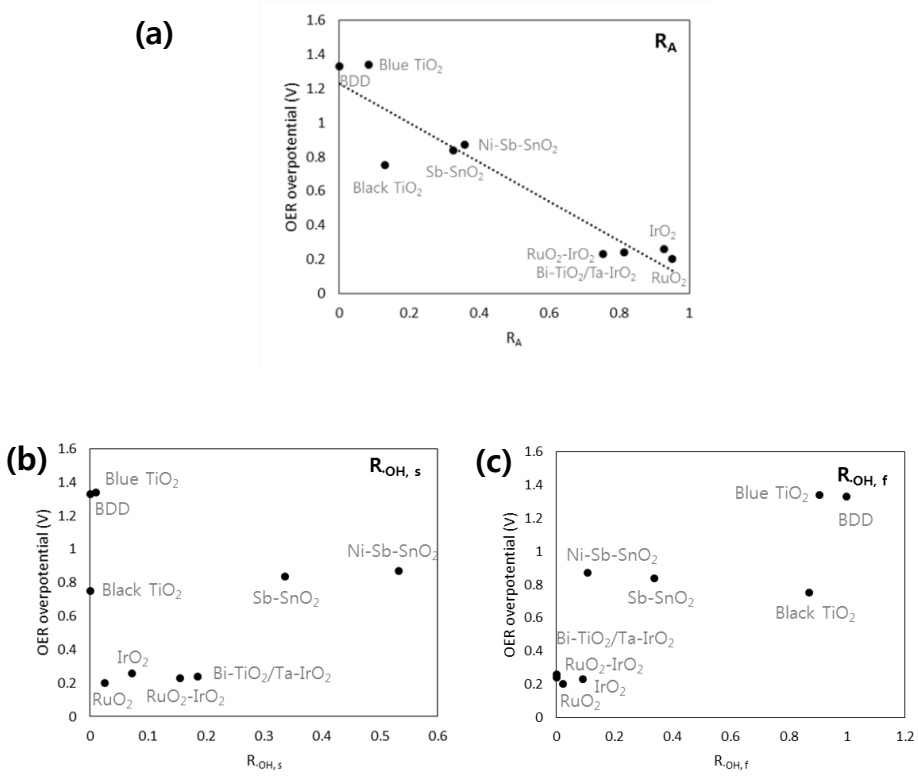

Figure 3-11. Relationship between oxygen evolution reaction (OER) overpotential and (a) R_A, (b) $R_{\cdot OH,s}$, and (c) $R_{\cdot OH,f}$.

R_A: Fraction of direct chlorine generation, $R_{\cdot OH,s}$: Fraction of surface adsorbed $^{\bullet}OH$ generation, and $R_{\cdot OH,f}$: Fraction of free $^{\bullet}OH$ generation (OER overpotential measurement: $[KH_2PO_4]_0$ = 0.1 M, scan rate 50 mV/s; fraction measurement: $[NaCl]_0$ = 0.1 M, $[t\text{-BuOH}]_0$ = 0.1 M, $[MeOH]_0$ = 0.1 M, 7 min, 16.7 mA cm^{-2}, pH 6.5, 25℃).

3.3.5. Classification and quantification of electrodes

Table 3-2 shows a summary of the results for the various types of electrodes classified according to the pathway for oxidant generation. As shown in Table 3-2, the active and inactive electrodes are precisely subdivided into three types using the results of Figure 3-9, and each electrode X is expressed according to the R_A, $R_{\cdot OH,s}$, and $R_{\cdot OH,f}$ as $X\{R_A, R_{\cdot OH,s}, R_{\cdot OH,f}\}$. For example, RuO_2 and blue TNA become $RuO_2\{0.95, 0.03, 0.02\}$ and blue TNA$\{0.08, 0.01, 0.91\}$, respectively. The active electrode is classified into $\{A\}$, and the inactive electrode is classified into two types, $\{I_{\cdot OH,s}\}$ and $\{I_{\cdot OH,f}\}$. This novel classification of electrodes is well consistent with the previous one which classified the DSA as the active electrode and BDD as the inactive electrode (Comninellis 1994, Cañizares et al. 2004, Rueffer et al. 2011). With this classification and quantification method, the characteristics of oxidant generating electrodes can be easily defined and classified not only for existing electrodes but also for novel electrodes reported.

Active Electrode	
{*A*} Electrode	RuO_2\{0.95, 0.03, 0.02\}
	IrO_2\{0.93, 0.07, 0\}
	Pt\{0.92, 0.06, 0.02\}
	Bi-TiO_2/Ta-IrO_2\{0.81, 0.19, 0\}
	RuO_2-IrO_2\{0.75, 0.16, 0.09\}
Inactive Electrode	
{$I_{\cdot OH,s}$&$I_{\cdot OH,f}$} Electrode	Ni-Sb-SnO_2\{0.36, 0.53, 0.11\}
	Sb-SnO_2\{0.33, 0.33, 0.34\}
{$I_{\cdot OH,f}$} Electrode	Black TNA\{0.13, 0, 0.87\}
	Blue TNA\{0.08, 0.01, 0.91\}
	BDD\{0, 0, 1\}

Table 3-2. Summary of the results for the various types of electrodes classified according to the pathways for oxidant generation.

3.4. Summary

This study proposes a novel quantitative classification method for oxidant generating electrodes according to three pathways for oxidant generation: direct chlorine generation, surface adsorbed $^{\bullet}$OH, and free $^{\bullet}$OH. All the electrodes examined in this study were classified according to the fraction of oxidant generating pathways as three types: The active electrode is classified into $\{A\}$, and the inactive electrode is classified into two types, $\{I_{\cdot OH,s}\}$ and $\{I_{\cdot OH,f}\}$. Moreover, the electrodes were quantitatively labeled such as $RuO_2\{0.93, 0.07, 0\}$ and blue TNA$\{0.04, 0.17, 0.79\}$, according to the fractions of $\{A\}$, $\{I_{\cdot OH,s}\}$ and $\{I_{\cdot OH,f}\}$. This novel classification method quantitatively defines the electrodes and also suggests new directions for developing innovative oxidant generating electrodes.

4. Types of Hydroxyl Radical for Electrochemical Peroxodisulfate (PDS) Generation

4.1. Introduction

Boron doped diamond (BDD) were widely used for peroxodisulfate (PDS) generation. However, there high price discourages its use in the field prompting the need for new electrode materials for PDS generation. On the other hand, recently, self-doped TiO_2 nanotube arrays (self-doped TNAs) have been shown to be a cost-effective electrode for generating oxidants (Kim et al. 2014, Kim et al. 2015). These self-doped TNAs have a high efficiency for the generation of $^{\bullet}OH$ and Cl_2 along with a high OER overpotential.

This study examine the potential of self-doped TNA electrodes (blue and black TNA electrodes) for PDS generation which are cheap and efficient for generating a significant amount of $^{\bullet}OH$ and comparable to BDD electrodes. To elaborate on the role of $^{\bullet}OH$ in PDS generation, *t*-butanol (*t*-BuOH) as a $^{\bullet}OH$ scavenger and *p*-chlorobenzoic acid (*p*CBA) as a $^{\bullet}OH$ probe compound were used to investigate self-doped TNA electrodes as electrode materials for PDS generation. Also, the types of $^{\bullet}OH$ (surface adsorbed or free) were examined from the relationship between electrode classification method and PDS generation.

4.2. Materials and Methods

4.2.1. Reagents

All chemicals were reagent grade and used without further purification. Chemicals used in this study include the following: Ethylene glycol, ammonium fluoride (NH_4F), sulfuric acid (H_2SO_4), potassium dihydrogen phosphate (KH_2PO_4), Perchloric acid ($HClO_4$), hydrogen chloride (HCl), ruthenium(III) chloride ($RuCl_3$), *tert*-butanol (*t*-BuOH), methanol (MeOH), potassium iodide (KI), sodium bicarbonate ($NaHCO_3$), *para*-chlorobenzoic acid (*p*CBA), and acetonitrile (all from Sigma–Aldrich Co.). All solutions were prepared in deionized water (Milli-Q ultrapure water-purification system, Millipore Co.). Stock solutions of KH_2PO_4 (1 M) and *p*CBA (0.26 mM) were prepared prior to use.

4.2.2. Preparation of the electrodes

Blue and black TNA electrodes, which have different doping levels, were chosen along with BDD, Sb-SnO_2, Ni-Sb-SnO_2 and RuO_2 to examine the characteristics of electrochemical PDS generation. Blue and black TNAs are formed as a result of the electrochemical activities by electrochemical self-doping on anatase TiO_2 with the cathodic polarization method (Kim et al. 2014, Kim et al. 2015, Kim et al. 2016). Black TNA has a higher doping level than that of blue TNA which means it has a large amount of Ti^{3+} sites (oxygen vacancies) (Kim et al. 2016). BDD, Sb-SnO_2, Ni-Sb-SnO_2 and RuO_2 were chosen to compare the electrochemical PDS generation with self-doped TNAs because BDD is a well-known PDS generating electrode, Sb-SnO_2 and Ni-Sb-SnO_2 generate the adsorbed $^{\bullet}OH$, and RuO_2 is known as a negligible $^{\bullet}OH$ generating electrode (Comninellis 1994, Kim et al. 2014, Kim et al. 2015).

Fabrication of the blue and black TNAs followed the anodization method described in previous studies (Kim et al. 2014, Kim et al. 2015). To fabricate blue TNA, a Ti plate was anodized at 40 V for 5 h in an ethylene glycol solution containing 0.2 wt% NH_4F and 2.5 wt% H_2O. Pristine TNA was prepared by anodizing a Ti plate annealed at 450 ℃ for 1 h in air. Then, the pristine TNA was cathodically polarized in KH_2PO_4 solution (0.1 M) at 16.7 mA cm^{-2} for 90 s to fabricate the blue TNA (Kim et al. 2014). Similarly, black TNA was fabricated as follows; a Ti plate was anodized under the same

conditions as those for the blue TNA and annealed at 200 ℃ for 1 h in air. Then, cathodic polarization was performed in KH_2PO_4 solution (0.1 M) at 16.7 mA cm^{-2} for 90 s. It was further annealed at 450 ℃ for 1 h under anoxic conditions (Kim et al. 2015).

Sb-SnO_2, Ni-Sb-SnO_2, and RuO_2 were fabricated with the thermal decomposition method as described in the previous studies (Le Luu et al. 2014, Yang et al. 2014). First, a Ti plate was polished with sand paper, etched in HCl at 80 ℃, and washed with deionized water. To fabricate the Sb-SnO_2 and Ni-Sb-SnO_2 coating solution of $SnCl_4 \cdot 5H_2O$, $SbCl_3$, and $NiCl_2 \cdot 6H_2O$ (0.1 M, respectively) were prepared as Sn:Sb atomic ratio of 95:5, and Sn:Sb:Ni atomic ratio of 95:5:1. The pre-treated Ti plate were dipped into the coating solution and annealed at 450 ℃ for 5 min. The dipping and annealing procedures were repeated 10 times and further annealed at 450 ℃ for 1 h (Yang et al. 2014). To prepare the RuO_2, 1.7 μmol cm^{-2} of Ru precursor (0.2 M $RuCl_3$) were dropped onto the pre-treated Ti plate. Then, RuO_2 was fabricated by annealing at 450 ℃ for 1 h (Le Luu et al. 2014). In the case of the BDD electrode, it was purchased from Condias GmbH, Germany.

4.2.3. Electrode characterization

The surfaces of the blue and black TNA electrodes fabricated in this study were analyzed with scanning electron microscopy (SEM, JSM-6700F, JEOL, Japan). The crystal structure was confirmed by High Resolution X-ray Diffractometer (XRD, D8DISCOVER, Bruker, Germany) using Cu Kα radiation (λ = 1.5406 Å).

Mott-Schottky plot was examined to obtain the doping level of the self-doped TNAs in KH_2PO_4 electrolyte (0.1 M, pH 7) with an AC potential of 10 mV and a frequency of 100 Hz. The doping level (N_D) was calculated by the inverse slope of the Mott-Schottky plot using Equation (4-1) (Bard et al. 2001):

$$\frac{1}{{C_{SC}}^2} = \left(\frac{2}{e\varepsilon\varepsilon_0 N_D}\right)\left(-(E - E_{fb}) - \frac{kT}{e}\right) \quad (4\text{-}1)$$

Here, C_{SC} is the space charge capacitance (F cm^{-2}); e is the electronic charge (1.6 x 10^{19} C); ε is the dielectric constant of the electrode material (ε(TiO_2) = 31) (Lu et al. 2012); ε_0 is the permittivity of the free space (8.86 x 10^{-14} F cm^{-1}); N_D is the donor density (cm^{-3}); E is the applied potential (V); E_{fb} is the flat band potential (V); *k* is the Boltzmann constant (1.38 x 10^{-23} J K^{-1}), and T is the operating temperature (298 K).

Cyclic voltammetry (CV) was measured to examine the electrochemical activity of the blue and black TNAs in H_2SO_4 (1 M) electrolyte with an Ag/AgCl (KCl sat`d) reference electrode with a scan rate of 10 mV/s. Current-overpotential curves for the self-doped TNAs were obtained by measuring staircase linear sweep voltammetry (SLSV) and corrected by IR compensation to examine the oxygen evolution reaction (OER) overpotential (Kapałka et al. 2008). SLSV was measured in KH_2PO_4 (1 M; pH 7) with a 50 mV step height and 1 min. step width. The ohmic drop was corrected by Eqs. (5)-(6):

$$\frac{\Delta\eta}{\Delta i} = \frac{b}{i} + R \tag{4-2}$$

$$\eta_{corr} = \eta - iR \tag{4-3}$$

Here, η is the overpotential (V); i is the current (A); b is the Tafel slope (V dec^{-1}), and R is the total areal specific uncompensated resistance (ohm cm^2). The total areal specific uncompensated resistance (R) was obtained from Equation (4-2) by the y-intercept of the $\Delta\eta/\Delta i$ vs. $1/i$ plot. The corrected overpotential (η_{corr}) was calculated by Equation (4-3).

4.2.4. Electrochemical experiments and analyses

PDS generation by electrolysis was carried out in a divided electrolytic cell with Nafion® 117 membrane to prevent the reduction of PDS under the cathodic environment. The anolyte was 50 mL of H_2SO_4 (1 M), and the catholyte was 70 mL of H_2SO_4 (1 M) with a constant current density (16.7 mA cm^{-2}). The anode had a working geometric area of 1.5 cm^2 (1 cm x 1.5 cm), and a same sized platinum mesh was used as the cathode. PDS generation was presented as the mean of three replicates with the standard deviation. In between the three replicates of PDS generation, blue TNA was cathodically polarized in KH_2PO_4 solution (0.1 M) at 16.7 mA cm^{-2} for 90 s, and other electrodes (black TNA, RuO_2, BDD) was used as prepared during all electrolysis. The PDS concentration was measured with a spectrophotometric method using potassium iodide at 352 nm by UV-vis spectroscopy (Agilent 8453, Agilent Life Sciences and Chemical Analysis, USA) after a 20 min reaction time (Liang et al. 2008, Lee et al. 2015).

The PDS generating current efficiency was calculated with Equation (4-4):

$$\text{Current efficiency } (\%) = \frac{C \times V \times n \times F}{I \times t} \times 100 \qquad (4\text{-}4)$$

Here, C is the PDS concentration (mol L^{-1}); V is the electrolyte volume (L); n is the number of electrons (1 mol eq^{-1}); F is the faradaic constant (96485 C eq^{-1}); I is the applied current (C s^{-1}), and t is the electrolysis time (s). The PDS

generation rate (M s^{-1}) is obtained from the slope of the time-concentration profile of the PDS generation.

Two methods were used to assess the effect of $^{\bullet}OH$ on the PDS generation. First, an excess amount of *t*-BuOH (0.1 M), a $^{\bullet}OH$ scavenger, was introduced into the electrochemical system, and the suppression of the PDS generation was quantified (Cho et al. 2005). Note that the level of scavenger concentration employed in this study (100 mM) is sufficient enough since the full effect of scavenging was achieved as exceeding 20 mM (Figure 4-5). Second, *p*CBA, a $^{\bullet}OH$ probe compound, was used to measure the $^{\bullet}OH$ generation by the rate constant for the *p*CBA degradation. The initial concentration of the *p*CBA was 1.92 μM in a KH_2PO_4 electrolyte (0.1 M). The degradation of the *p*CBA was analyzed by HPLC (YL9100, Younglin Co., Korea) with UV absorbance detection at 230 nm. For the HPLC analysis, 40 mM aqueous solution of KH_2PO_4 and acetonitrile at a ratio of 65:35 ((v/v) mixture) was used as the mobile phase (flow rate = 1.0 mL/min) with an Agilent - Eclipse XDB C18 column (150 x 4.6 mm, 5 μm) (Elovitz et al. 1999). The *p*CBA degradation is presented as the mean of three replicates with the standard deviation. The electrodes were operated in the same manner as in PDS generation experiment.

To examine the effect of direct one-electron oxidation of HSO_4^- in making $SO_4^{-\bullet}$ (Reaction (2-15)), 0.01 M, 0.02 M, and 0.1 M of scavengers (*t*-BuOH

and MeOH) were introduced into the electrochemical PDS generation system, and the suppression of the PDS generation rate was quantified. The *t*-BuOH mainly suppresses the $^{\bullet}OH$ and insensitive to $SO_4^{-\bullet}$ while the MeOH scavenges both the $^{\bullet}OH$ and $SO_4^{-\bullet}$ (Buxton et al. 1988, Clifton et al. 1989, Farhat et al. 2015).

4.3. Results and Discussion

4.3.1. Electrode characterization

Figure 4-1 shows the photographs, the XRD patterns, and the SEM images of the blue and black TNAs. As seen in Figure 4-1(a), the blue and black TNAs had a blue and black color, respectively. Figure 4-1(b) shows the crystal structures of the self-doped TNAs with the characteristic peak positions of the XRD patterns. Both the blue and black TNAs corresponded well to the anatase TiO_2 structure (JCPDS 84-1286, marked as "A" in Figure 4-1(b)), and there was no difference between the blue and black TNAs. The peaks in the blue and black TNAs, which do not fit with the anatase TiO_2, are the metallic Ti peaks (marked as "T" in Figure 4-1(b)).

The blue and black TNAs have uniform nanotube structures with tube diameters and tube wall thicknesses of around 80 and 10-20 nm (Figure 4-1(c)), respectively. All the characteristics regarding the crystal and surface structures of the self-doped TNAs were well consistent with those reported in previous studies (Kim et al. 2014, Kim et al. 2015).

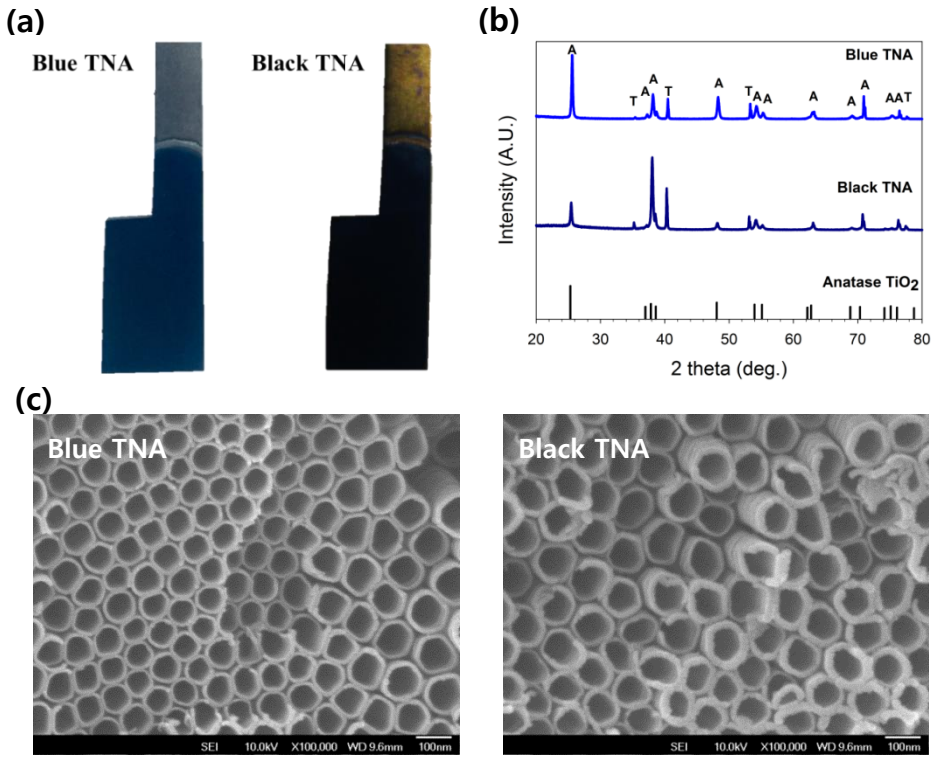

Figure 4-1. (a) Photographs of the blue and black TNAs, (b) structure characterization of the self-doped TNAs with XRD patterns and (c) SEM images.

The XRD patterns of the blue and black TNAs were indexed with reference to the JCPDS file (Card # 84-1286). The “A” and “T” in the XRD pattern indicate anatase and titanium, respectively.

Figure 4-2 shows the electrochemical characteristics of the blue and black TNAs with (a) the Mott-Schottky plot and (b) cyclic voltammetry for the self-doped TNAs. The doping level can be calculated from the inverse slope of the Mott-Schottky plot, and the cyclic voltammetry shows the electrochemical activity. As seen in Figure 4-2(a), the anatase TiO_2 has the highest slope followed by the blue and black TNAs which means that the doping level was increased in the blue TNA (2.1×10^{21} cm^{-3}) and black TNA (2.2×10^{23} cm^{-3}) compared to the pristine TNA (6.1×10^{20} cm^{-3}). The black TNA has a higher doping level than that of the blue TNA which is consistent with the previous results (Kim et al. 2016).

Figure 4-2(b) shows the cyclic voltammograms of the blue and black TNAs. As seen in Figure 4-2(b), OER occurred on the self-doped TNAs while the pristine TNA exhibited no electrochemical activity indicating that the blue and black TNAs can be used as electrodes, and pristine TNA is a non-conductive material not suitable for electrodes. A current increase by direct oxidation of SO_4^{2-} to PDS (1.88 V vs. Ag/AgCl) was not observed on the cyclic voltammogram indicating negligible PDS generation by direct electron transfer on the electrode surface, as similarly observed in the BDD electrode (Davis et al. 2014).

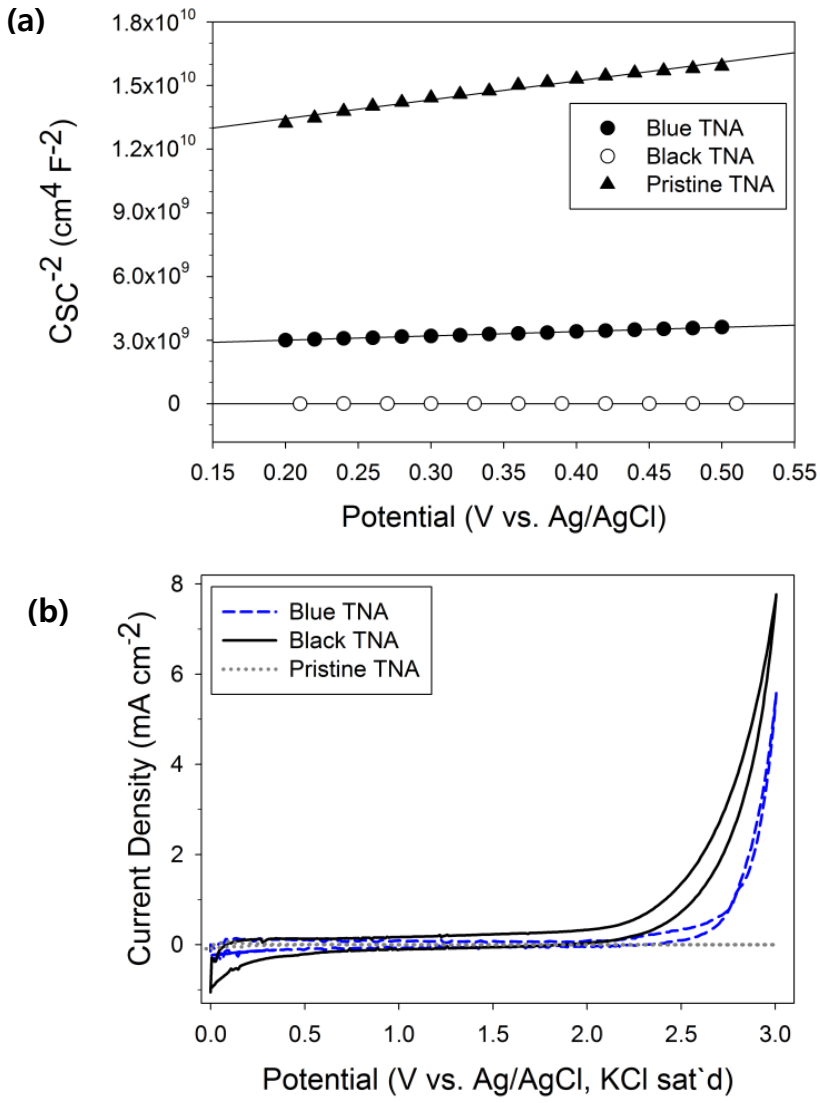

Figure 4-2. (a) Mott-Schottky plot and (b) cyclic voltammetry of self-doped TNAs.

(Mott-Schottky plot: $[KH_2PO_4]_0$ = 0.1 M, pH 7, 20 ℃, 10 mV, 100 Hz; cyclic voltammetry: $[H_2SO_4]_0$ = 1 M, pH 0, 20 ℃, 10 mV s^{-1}).

4.3.2. PDS Generation on self-doped TNAs and role of •OH

Figure 4-3 shows the electrochemical generation of PDS (time-concentration profile (a) and current efficiency (b), during 30 min.) on the blue and black TNA electrodes compared with the BDD, Sb-SnO_2, Ni-Sb-SnO_2 and RuO_2 electrodes. As shown in Figure 4-3(a), the PDS concentration linearly increased according to the electrolysis time for all the electrodes except for the Ni-Sb-SnO_2 and RuO_2, implying that the decomposition of PDS is negligible during electrolysis. Especially, the blue TNA generated the highest concentration of PDS (2.0 mM at 30 min.) followed by BDD (1.7 mM at 30 min), black TNA (1.1 mM at 30 min.) and Sb-SnO_2 (0.46 mM at 30 min.). Note the negligible generation of PDS in the case of Ni-Sb-SnO_2 and RuO_2 (0.01 mM at 30 min. in both electrodes) (Jeong et al. 2009).

Figure 4-3(b) shows that the PDS generating current efficiency during 30 min. was the highest for the blue TNA at 46% followed by BDD at 41% and black TNA at 22%, Sb-SnO_2 at 10% and below 1% for Ni-Sb-SnO_2 and RuO_2. The PDS generating current efficiency for the blue TNA (46%) is as high as that of the BDD which has been reported for the PDS generating electrode in previous studies (20-47%, H_2SO_4 electrolyte at 20-25 ℃) (Michaud et al. 2000, Davis et al. 2014, Davis et al. 2014). As shown in Figure 4-3, blue TNA is more efficient than black TNA for PDS generation. This efficient PDS

generation of blue TNA is explained by its superior generation of $^{\bullet}OH$ (Figure 4-4 and Figure 4-6), since PDS is generated from the reaction with $^{\bullet}OH$.

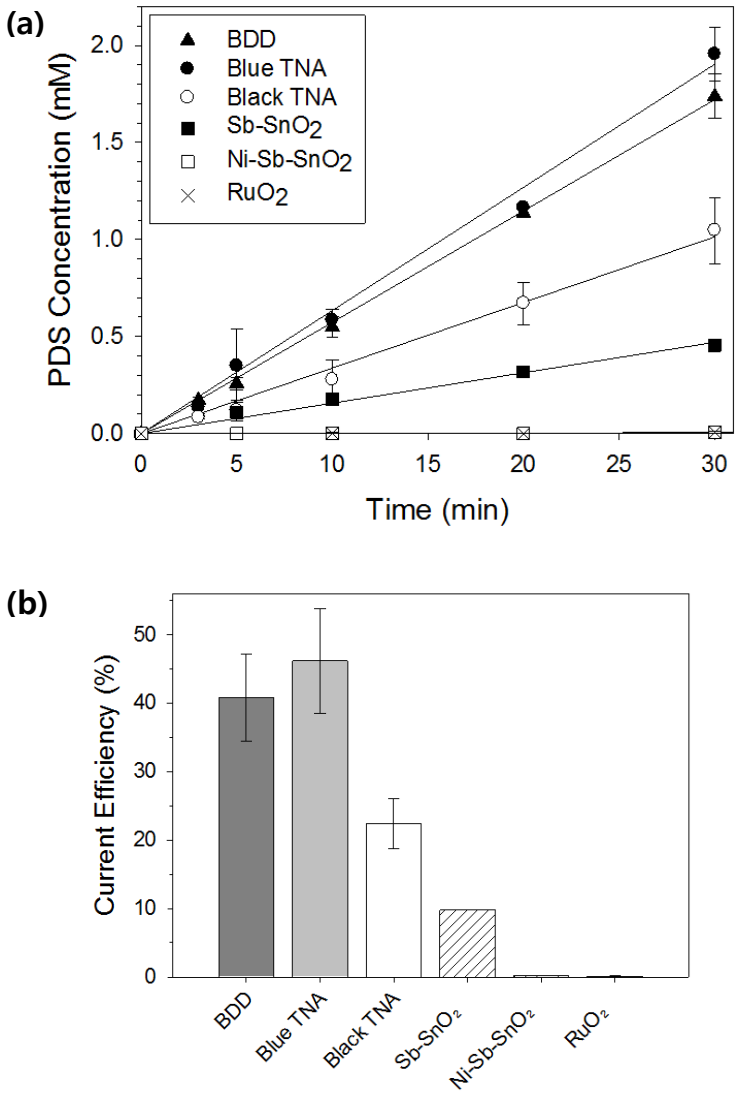

Figure 4-3. PDS generation on the blue and black TNA electrodes compared with the BDD, Sb-SnO_2, Ni-Sb-SnO_2 and RuO_2 electrodes.

(a) Generated PDS concentration, and (b) current efficiency for PDS generation at 30 min. ($[H_2SO_4]_0$ = 1 M, 16.7 mA cm^{-2}, pH 0, 20 ℃).

4.3.3. Role of •OH for PDS generation on self-doped TNAs

Figure 4-4 explains the role of •OH regarding the PDS generation on the self-doped TNAs as it was examined in the presence of a •OH scavenger (*t*-BuOH) and •OH probe compound (*p*CBA). As seen in Figure 4-4(a), PDS generation was almost completely suppressed, up to by 95-100% on the self-doped TNAs and BDD electrodes in the presence of *t*-BuOH, indicating that •OH is the precursor for PDS generation. Figure 4-4(b) shows the *p*CBA degradation on the four electrodes. The *p*CBA degradation in a log scale exhibited linearity with time following pseudo first-order kinetics. The slope of the plot represents the rate constant for the *p*CBA degradation (k_{exp}) which corresponds to •OH generation. The rate of the *p*CBA degradation was in the order of Ni-Sb-SnO_2 > blue TNA > BDD > black TNA > Sb-SnO_2 > RuO_2. •OH generation properties on blue and black TNAs were also reported on the previous studies (Kim et al. 2014, Kim et al. 2015, Kim et al. 2016).

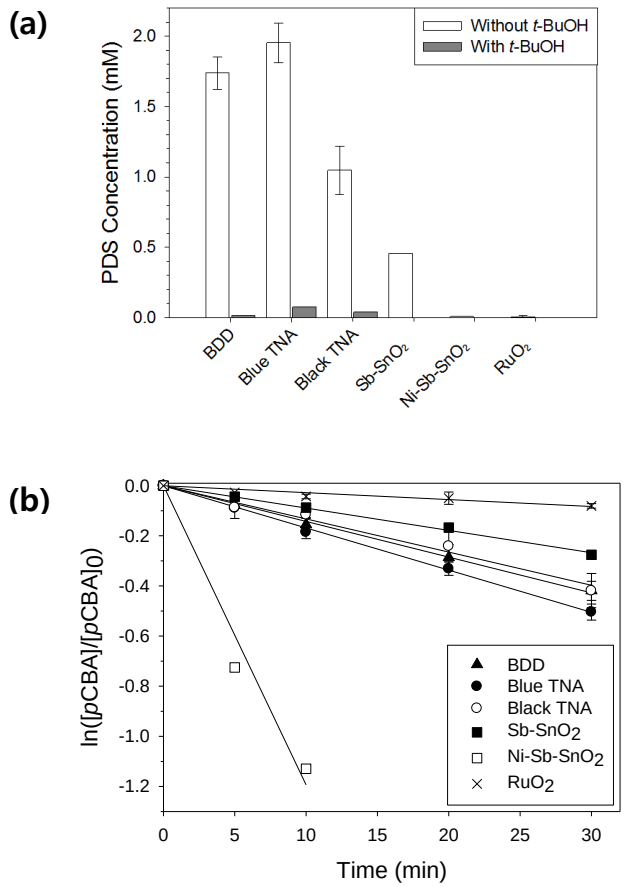

Figure 4-4. Role of •OH in PDS generation on the self-doped TNAs examined by (a) PDS generation with *t*-BuOH as a •OH scavenger, (b) degradation of *p*CBA (a •OH probe compound).

(PDS generation: $[H_2SO_4]_0$ = 1 M, $[t\text{-BuOH}]_0$ = 0.1 M, 30 min. electrolysis, 16.7 mA cm^{-2}, pH 0, 20 ℃; *p*CBA degradation: $[KH_2PO_4]_0$ = 0.1 M, $[p\text{CBA}]_0$ = 1.92 μM, 16.7 mA cm^{-2}, pH 7, 20 ℃).

In order to confirm the $^{\bullet}OH$ is the predominant precursor for PDS generation, PDS generation rate was measured in several different concentrations of scavengers of interest (*t*-BuOH and MeOH) by excluding the direct one-electron oxidation of HSO_4^- (Reaction (2-15)) (Figure 4-5). As shown in Figure 4-5, PDS generation rate shows similar scavenging effect in MeOH with that of *t*-BuOH as the scavengers were employed with respect to concentration, indicating that the direct electrolysis of HSO_4^- to $SO_4^{-\bullet}$ is negligible. Note that *t*-BuOH suppresses the $^{\bullet}OH$, although it is not reactive to $SO_4^{-\bullet}$, while MeOH scavenges both the $^{\bullet}OH$ and $SO_4^{-\bullet}$ (Buxton et al. 1988, Clifton et al. 1989, Farhat et al. 2015). That is, the reaction of $^{\bullet}OH$ with HSO_4^- is the dominant pathway for $SO_4^{-\bullet}$ generation.

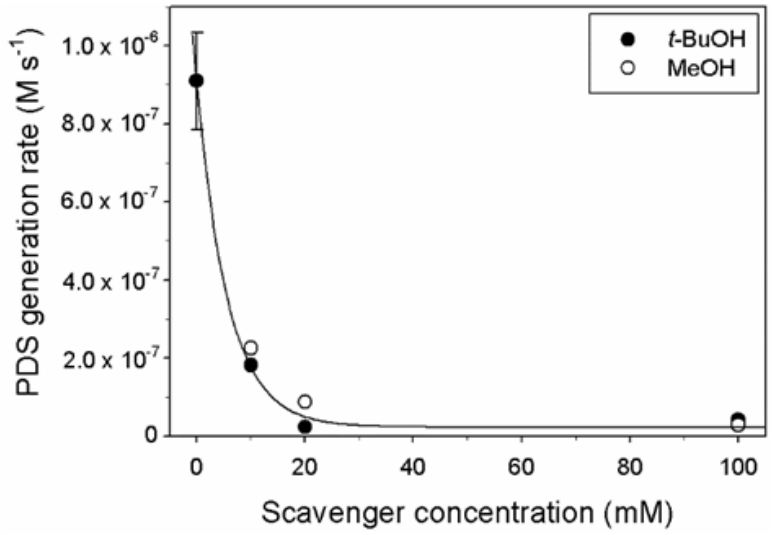

Figure 4-5. Effect of *t*-BuOH and MeOH to PDS generation rate on blue TNA.

($[H_2SO_4]_0$ = 1 M, $[t\text{-BuOH}]_0$ and $[MeOH]_0$ = 10, 20, and 100 mM, 30 min. electrolysis, 16.7 mA cm^{-2}, pH 0, 20℃).

Figure 4-6 shows the relationship between the $I_{\cdot OH,s}$ or $I_{\cdot OH,f}$ concentration measured by the chlorine and PDS concentration. $I_{\cdot OH,s}$ and $I_{\cdot OH,f}$ means the surface adsorbed or free $^{\bullet}$OH, respectively, which was measured with chlorine concentration when the *t*-BuOH and MeOH was added. $I_{\cdot OH,s}$ and $I_{\cdot OH,f}$ concentrations were obtained from the Chapter 3. As shown in Figure 4-6(a), the PDS concentration is linearly related to concentration of $I_{\cdot OH,f}$ with R^2 = 0.90. This implies that the PDS is generated from the free $^{\bullet}$OH not from the surface adsorbed $^{\bullet}$OH. It is also supported by the Figure 4-4 which shows that PDS generation on Ni-Sb-SnO_2 was negligible (Figure 4-4(a)) although Ni-Sb-SnO_2 generate the $^{\bullet}$OH with high rate constant compare to that of blue TNA, black TNA and BDD (Figure 4-4(b)). This is contradictory to previous studies which explains that the high PDS generation result from the superior $^{\bullet}$OH generating properties. The result of Figure 4-4 can be explained with the Figure 4-6. Because the free $^{\bullet}$OH is the precursor for PDS generation, free $^{\bullet}$OH generating electrodes such as blue TNA, black TNA and BDD exhibit the high performance for PDS generation while the Ni-Sb-SnO_2 generates the negligible amount of PDS because Ni-Sb-SnO_2 is the surface adsorbed $^{\bullet}$OH generating electrode. Figure 4-6(b) shows that there is no relationship between the surface adsorbed $^{\bullet}$OH and PDS generation. Also, as shown in Figure 4-6(c), there are less relationship between the total $^{\bullet}$OH generation and PDS generation.

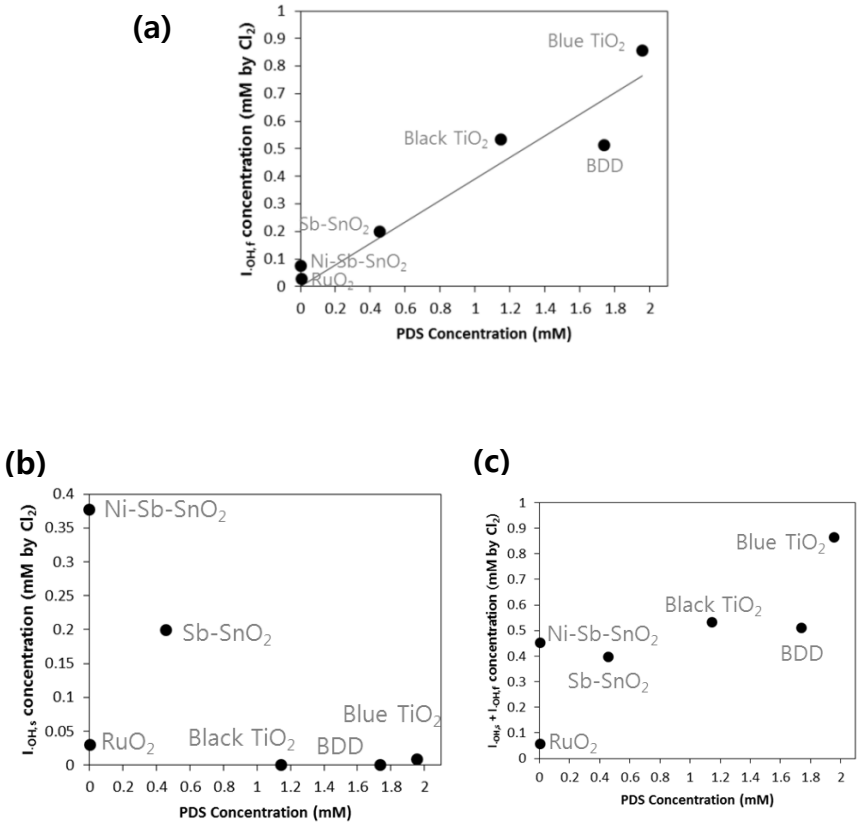

Figure 4-6. The relationship between the $I_{\cdot OH,s}$ or $I_{\cdot OH,f}$ concentration concentration measured by the chlorine and PDS concentration.

$I_{\cdot OH,s}$ and $I_{\cdot OH,f}$: surface adsorbed or free $^{\bullet}OH$, respectively. (PDS generation: $[H_2SO_4]_0$ = 1 M, [*t*-BuOH]$_0$ = 0.1 M, 30 min. electrolysis, 16.7 mA cm^{-2}, pH 0, 20 ℃; $I_{\cdot OH,s}$ or $I_{\cdot OH,f}$ concentration: $[NaCl]_0$ = 0.1 M, [*t*-BuOH]$_0$ = 0.2 M, $[MeOH]_0$ = 0.2 M, 16.7 mA cm^{-2}, pH 6, 20 ℃).

4.4. Summary

This study reported that self-doped TiO_2 nanotube array electrodes (blue and black TNA electrodes) as cost-effective alternatives to the BDD electrode are suitable for PDS generation. The blue TNA electrode exhibited an excellent PDS generating property with a high current efficiency for PDS generation (46%) which was superior to that of BDD (41%). In addition, it was confirmed that free $^{\bullet}OH$ was the key precursor for PDS generation evident by the suppression of PDS generation in the presence of a $^{\bullet}OH$ scavenger and $^{\bullet}OH$ generation as well as by the linear correlation of the PDS generation and electrode classification. The results obtained by this study indicate that self-doped TNA electrodes (particularly blue TNA), as cost-effective alternatives to BDD electrode for generation of PDS, can be suitably applied to various industrial fields where PDS is used. Also, not only self-doped TNAs but also other free $^{\bullet}OH$ generating electrodes have the possibility to be used for PDS generation.

5. RuO_2 Coated Blue TiO_2 Nanotube Array (Blue TNA-RuO_2) as an Effective Anode Material in Electrochemical Chlorine Generation

5.1. Introduction

Chlorine generation is one of the largest processes of electrochemistry (Trasatti 1984, Trasatti 1987, Hansen et al. 2010, Over 2013, Le Luu et al. 2014). Especially, the anode material is a significant factor for the electrochemical chlorine generation process (Over 2013). Dimensionally stable anode (DSA) and boron doped diamond (BDD) are the most widely used electrodes for the generation of oxidants and are known to have different pathways for chlorine generation. DSA is a typical anode material for electro-chlorination and has been studied for decades to increase the chlorine generation efficiency (Ferro et al. 2002, Guerrini et al. 2005, Hansen et al. 2010, Over 2013, Le Luu et al. 2014). The DSA electrode is known as an active electrode which has a low overpotential for chlorine generation. It produces chlorine by the direct oxidation of chloride ions on the electrode surface. The pathways for the direct oxidation of chloride are shown in Reaction (5-1) and (5-2) where S means the electrode surface (Trasatti 1984, Trasatti 1987, Fernández et al. 2002, Over 2013, Kim et al. 2015).

$$S + Cl^- \rightleftarrows S\text{-}Cl + e^- \qquad (5\text{-}1)$$

$$S\text{-}Cl + Cl^- \rightleftarrows S + Cl_2 \quad (5\text{-}2)$$

Chloride ions are first adsorbed onto the electrode surface by discharging one electron (Reaction (5-1)). Then, the adsorbed chloride reacts with the chloride ion to generate the chlorine (Reaction (5-2)). This mechanism is known as direct chlorine generation because the chloride ion transfers the electron directly to the electrode surface. BDD was reported as an inactive electrode which has a high overpotential for oxygen generation so that the chlorine is generated indirectly from the reaction of the hydroxyl radical ($^{\bullet}OH$) and chloride ion (Comninellis 1994, Marselli et al. 2003, Panizza et al. 2005, Kim et al. 2015). This pathway is shown in Reaction (5-3) and (5-4).

$$S + H_2O \rightarrow S(^{\bullet}OH) + H^+ + e^- \quad (5\text{-}3)$$

$$2^{\bullet}OH + 2Cl^- \rightarrow 2OH^- + Cl_2 \quad (5\text{-}4)$$

The electrode surface acts as an electrocatalyst for the decomposition of water, and the $^{\bullet}OH$ is generated (Reaction (5-3)). The generated $^{\bullet}OH$ reacts with the chloride ion in the electrolyte to generate the chlorine (Reaction (5-4)). This procedure is known as indirect chlorine generation. Although DSA and BDD were developed over the last few decades, DSA uses costly materials such as ruthenium and iridium which are a burden on the production cost. On the other hand, the BDD fabrication procedure uses chemical vapor deposition (CVD), which limits the application of BDD only to small scale electrolysis.

Recently, blue TiO_2 nanotube array (blue TNA) was reported as an anode material which uses the cost-effective TiO_2 and has a simple fabrication method (Kim et al. 2014, Kim et al. 2016, Kim et al. 2016). Blue TNA exhibits a high electrocatalytic activity for chlorine and $^{\bullet}OH$ generation, which is comparable to DSA and BDD, respectively. Blue TNA was reported as a dominantly inactive electrode with which chlorine is generated indirectly from the reaction between the $^{\bullet}OH$ and chloride ion (Kim et al. 2014). However, the indirect pathway of the blue TNA leads to a slightly lower efficiency in chlorine generation compared with that of DSA, which requires further research to enhance the chlorine generating efficiency for industrial applications (Kim et al. 2014).

In this study, a novel electrode was fabricated by coating RuO_2 onto the blue TNA (blue TNA-RuO_2) to increase the chlorine generation of blue TNA using the direct and indirect pathways simultaneously on one electrode. The chlorine generation was studied on the blue TNA-RuO_2 electrode and compared to RuO_2 and blue TNA electrodes. Additionally, the direct and indirect oxidation pathways were investigated with a probe compound and scavenger for $^{\bullet}OH$.

5.2. Materials and Methods

5.2.1. Reagents

All chemicals were reagent grade and used without further purification. All solutions were prepared in deionized water (Milli-Q® Direct 8 system, Millipore, USA, <18 MΩ·cm). Chemicals used in this study included the following: Ruthenium chloride ($RuCl_3$), hydrochloric acid (HCl), ethylene glycol, ammonium fluoride (NH_4F), ethanol, potassium hydrogen phosphate (KH_2PO_4), sodium chloride (NaCl), *p*-nitrosodimethylaniline (RNO), and *t*-butanol (*t*-BuOH) (all from Sigma–Aldrich Co.). Titanium foil with a 0.25 μm thickness (Sigma-Aldrich Co.) was used to fabricate the electrodes.

5.2.2. Preparation of the electrodes

Blue TNA-RuO_2, blue TNA, and RuO_2 were fabricated as anodes with a 6 cm^2 (2 x 3 cm) working area, and the cathode was platinum foil with the same size. To fabricate the blue TNA-RuO_2, first blue TNA was fabricated with the anodization method, and then, RuO_2 was coated onto the blue TNA by the thermal decomposition method (Kim et al. 2001, Kim et al. 2014, Le Luu et al. 2014). Ti foil was anodized for 16 h in ethylene glycol which contained H_2O (2.5 wt%)/NH_4F (0.2 wt%), and TNA was fabricated. A DC power supply (UDP-150I, Unicorn Tech Co., Korea) was used to provide a constant potential (45 V). The prepared TNA was washed with ethanol and annealed at 450 ^oC for 1 h in air. Then, Ru precursor (0.2 M $RuCl_3$), which was dissolved in HCl and DI at 1:1 (v/v), was loaded onto the annealed TNA and annealed again at 450 ^oC for 1 h in air to crystalize the RuO_2. The electrode was post-treated with the cathodic polarization method in phosphate buffer solution ($[KH_2PO_4]_0$ = 0.1 M, pH = 7.2) under a constant cathodic current (16.7 mA cm^{-2}) for 90 s.

The blue TNA electrode was fabricated by the anodization method, and RuO_2 was fabricated by the thermal decomposition method as previously described (Kim et al. 2001, Kim et al. 2014, Le Luu et al. 2014). The Ru content was controlled as 1.7 μmol cm^{-2} in both the blue TNA-RuO_2 and RuO_2 electrodes.

5.2.3. Characterization of the electrodes

The surfaces of the blue TNA-RuO_2, blue TNA, and RuO_2 electrodes were characterized by scanning electron microscopy (SEM, JSM-6700F, JEOL, Japan). The crystal structure of the prepared electrodes was determined by a high resolution X-ray diffractometer (XRD, D8DISCOVER, Bruker, Germany). Cyclic voltammetry (CV) was measured to confirm the electrochemical activity of the blue TNA-RuO_2, blue TNA, and RuO_2 in a NaCl (0.1 M) electrolyte with a Ag/AgCl (KCl sat`d) reference electrode at a scan rate of 100 mV s^{-1}..

5.2.4. Electrochemical experiments and analyses

Generation of oxidants on the blue TNA-RuO_2 electrode was compared with that of the blue TNA and RuO_2 electrodes. All results of the experiments are presented as the mean of three replicates with the standard deviation. For chlorine generation, a current density of 16.7 mA cm^{-2} was applied in 150 mL of a 0.1 M NaCl electrolyte. The concentration of chlorine was measured as the total chlorine using the *N*,*N*-diethyl-*p*-phenylenediamine (DPD) method at 530 nm with a spectrophotometer (DR/2010, HACH Co., USA). The current efficiency for chlorine generation was calculated with Equation (5-5).

$$\text{Current efficiency (\%)} = \frac{V \cdot C \cdot n \cdot F}{i \cdot t} \times 100 \quad (5\text{-}5)$$

Here, i is the applied current (C s^{-1}); t is the time (s); V is the electrolyte volume (L); C is the chlorine concentration (mol L^{-1}); n is the number of electrons (2 mol eq^{-1}), and F is the faradaic constant (96485 C eq^{-1}). Energy consumption for generating 1 g of chlorine was calculated with Equation (5-6).

$$\text{Energy consumption (Wh } g^{-1}) = \frac{i \cdot E \cdot t}{c \cdot V} \quad (5\text{-}6)$$

Here, i is the applied current (A); E is the voltage (V); t is the time (h); c is the chlorine concentration (g L^{-1}), and V is the electrolyte volume (L).

To estimate the $^{\bullet}OH$ generation, the RNO bleaching method was used with UV-vis spectroscopy (Agilent 8453, Agilent Life Sciences and Chemical

Analysis, USA). RNO is well known as a probe compound to estimate the •OH generation (Iniesta et al. 2001, Kim et al. 2013). The bleaching reaction of RNO with •OH, which was assumed to follow pseudo-first order kinetics, can be expressed with Equation (5-7).

$$-\frac{d[RNO]}{dt} = k[^{\bullet}\mathrm{OH}]_{ss}[RNO] = k_{obs}[RNO] \quad (5\text{-}7)$$

From the integration of Equation (5-7),

$$-ln\frac{[RNO]}{[RNO]_0} = k_{obs}t \quad (5\text{-}8)$$

, where $k_{obs} = k[^{\bullet}OH]_{ss}$; $k = 1.25\times10^{10}\ M^{-1}s^{-1}$ (Simonsen et al. 2010); $[RNO]_0$ = initial concentration of RNO; [RNO] = concentration of RNO, and $[^{\bullet}OH]_{ss}$ = steady state concentration of •OH. The semi-log plot was obtained from the assumption of the pseudo-first order kinetics (Equation (5-7)) with the concentration of RNO calculated from the absorbance spectra (440 nm). The linearity of the slope in the semi-log plot (Equation (5-8)) indicates the concentration of •OH is in steady state. The effect of the •OH in chlorine generation was evaluated by the scavenging test using 1 M *t*-BuOH.

.

5.3. Results and Discussion

5.3.1. Electrode characterization

Figure 5-1 shows the surface of the (a) blue TNA-RuO_2, (b) blue TNA, and (c) RuO_2 examined by SEM, and (d) the XRD patterns. As shown in Figure 5-1(a), the blue TNA-RuO_2 exhibited a well-organized TNA with an 80 nm pore diameter, which is the same structure as the blue TNA (Figure 5-1(b)). In the blue TNA-RuO_2 electrode, the RuO_2 is well coated onto the top of the blue TNA, and nanopores in the TNA are partially blocked. The surface structure of the RuO_2 (Figure 5-1(c)) and blue TNA (Figure 5-1(b)) is consistent with previous results (Kim et al. 2014, Luu et al. 2015).

Figure 5-2 shows the crystal structures of the blue TNA-RuO_2, blue TNA, and RuO_2 with the characteristic peak positions of the XRD patterns. For the blue TNA-RuO_2 electrode, both the anatase TiO_2 and RuO_2 peaks were observed, which are marked as A and R, respectively. That is, the blue TNA and RuO_2 retain their crystal structures in the blue TNA-RuO_2 without structural changes or formation of solid solutions which can be observed by a peak shift. Blue TNA showed the anatase TiO_2 crystal structure (JCPDS 84-1286), and the RuO_2 corresponded to the rutile RuO_2 structure (JCPDS 88-0323).

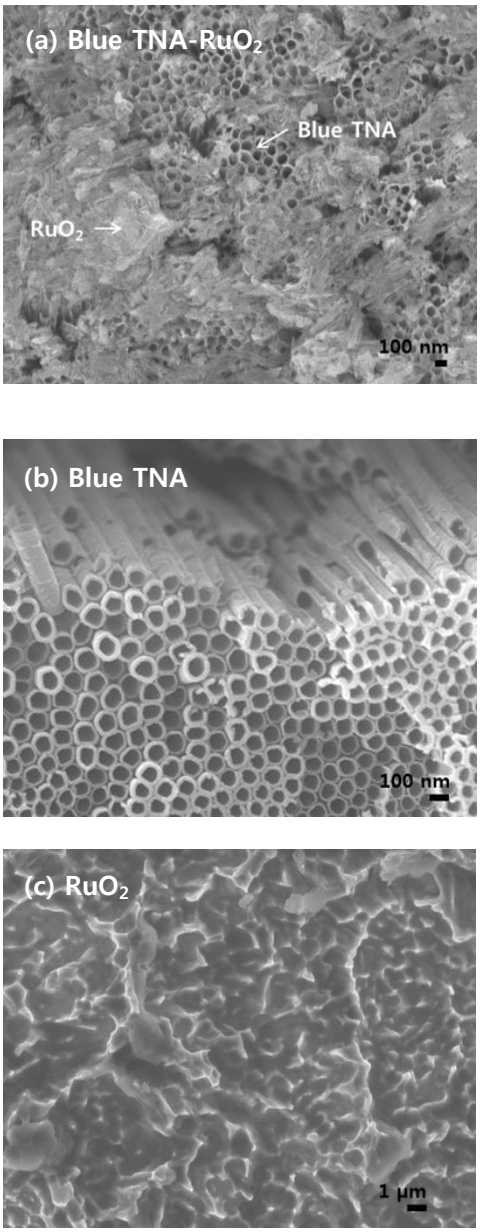

Figure 5-1. Electrode characterization with SEM images of the (a) blue TNA-RuO_2, (b) blue TNA, and (c) RuO_2

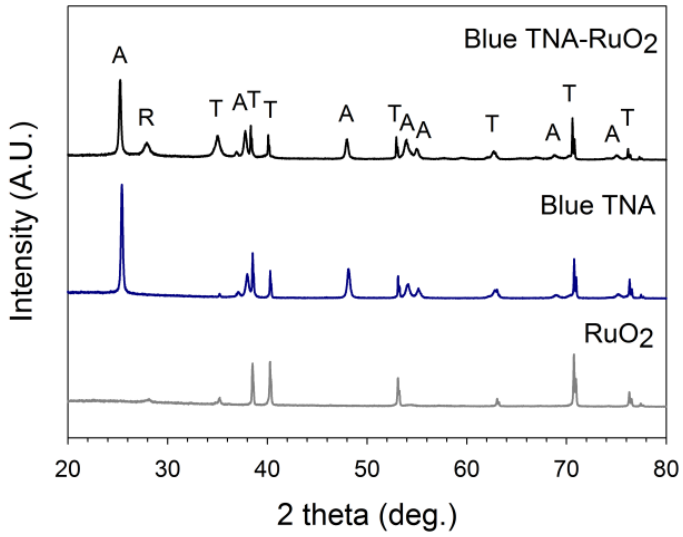

Figure 5-2. Structure characterization of the blue TNA-RuO_2 with XRD patterns.

The XRD patterns were indexed with the reference to the JCPDS file (Card # 84-1286 for anatase TiO_2 and 88-0323 for rutile RuO_2). The A, R, and T in the XRD pattern indicate anatase TiO_2, RuO_2, and titanium metal, respectively.

.

5.3.2. Chlorine generation on the blue TNA-RuO_2 electrode

Figure 5-3 shows the chlorine generation, current efficiency, and energy consumption of the blue TNA-RuO_2 compared with the blue TNA and RuO_2. As shown in Figure 5-3(a), the blue TNA-RuO_2 generated the highest concentration of chlorine (99 mg L^{-1} at 7 min) followed by the RuO_2 (84 mg L^{-1} at 7 min) and the blue TNA (77 mg L^{-1} at 7 min). The chlorine concentration linearly increased according to the electrolysis time for all electrodes. That is, the surface reaction rate for chlorine generation is constant during the electrolysis which means the migration of chloride ions to the electrode surface is continuous and is not restricted by the surface structure even within the nanotubes on the blue TNA-RuO_2 and blue TNA electrodes. Figure 5-3(b) shows the current efficiency and energy consumption for the chlorine generation on the blue TNA-RuO_2 compared with those of the blue TNA and RuO_2. As shown in Figure 5-3(b), the chlorine generating current efficiency of the blue TNA-RuO_2 was the highest at 96% (with a 7 min. electrolysis at 0.1 M NaCl electrolyte). The chlorine generating current efficiency was 82% for the RuO_2 and 74% for the blue TNA. The chlorine generating current efficiency for the blue TNA and RuO_2 was within the range of those reported in previous studies (Trasatti 1984, Choi et al. 2013, Over 2013, Kim et al. 2014, Le Luu et al. 2014). Figure 5-3(b) shows the energy consumption for the chlorine generation on the blue TNA-RuO_2 compared with that of the blue TNA and

RuO_2. The energy consumption for generating 1 g of chlorine on the blue TNA-RuO_2 was 3.2 Wh g^{-1}, which was similar to that of the RuO_2 (3.3 Wh g^{-1}), while the blue TNA consumed 6.2 Wh g^{-1} of energy in the same condition. The energy consumption is decreased for the blue TNA-RuO_2 electrode compared with the blue TNA, which is a result of the high current efficiency of the blue TNA-RuO_2 because of the synergetic effect of the blue TNA and RuO_2.

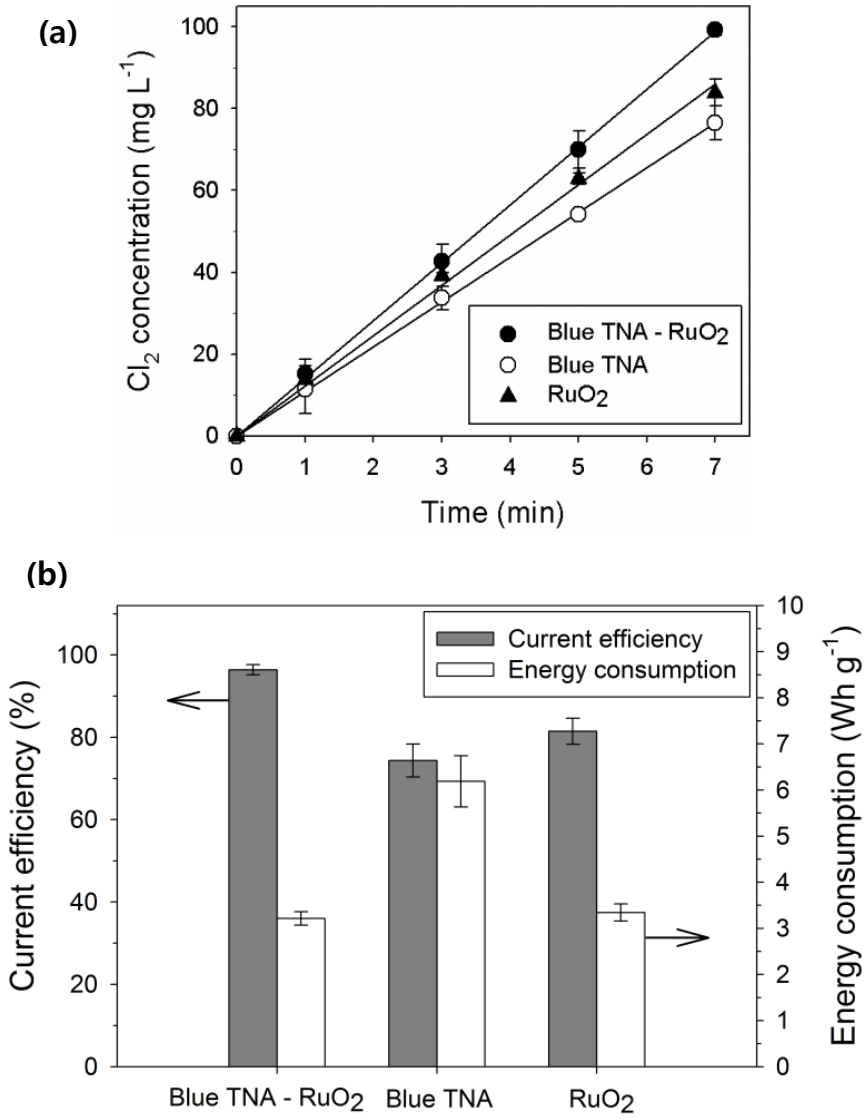

Figure 5-3. Chlorine generation, current efficiency, and energy consumption of the blue TNA-RuO_2 compared with the blue TNA and RuO_2.

(a) Chlorine generation, (b) current efficiency, and energy consumption ($[NaCl]_0$ = 0.1 M, 16.7 mA cm^{-2}, electrolysis time 7 min, pH 6, 25℃).

5.3.3. Direct and indirect pathways of chlorine generation on the blue TNA-RuO_2

Figure 5-4 shows the chlorine generation with *t*-BuOH as a •OH scavenger. Chlorine generation was suppressed by 22% on the blue TNA-RuO_2 electrode in the presence of *t*-BuOH indicating that the generated chlorine through the indirect oxidation of Cl^- ions by •OH affects the total chlorine generation along with the direct chlorine generation pathway. In the case of the blue TNA, 82% of the chlorine was decreased when *t*-BuOH was added, and chlorine was mostly generated by the indirect pathway. On the other hand, there is no •OH scavenging effect on the RuO_2 electrode, which means the chlorine is generated only with the direct pathway on the RuO_2 electrode. Figure 5-4 implies that the blue TNA part in the blue TNA-RuO_2 electrode was not fully utilized because part of the blue TNA was covered while the coated RuO_2 is dominantly affected to increase the chlorine generation on the blue TNA-RuO_2 electrode.

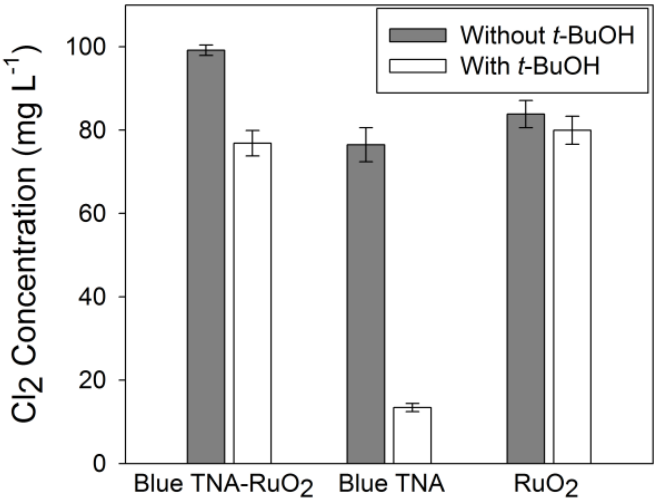

Figure 5-4. Chlorine generation pathway on the blue TNA-RuO_2 compared with the blue TNA and RuO_2 examined by chlorine generation with *t*-BuOH as a $^{\bullet}OH$ scavenger.

($[NaCl]_0$ = 0.1 M, $[t\text{-BuOH}]_0$ = 1 M, 7 min. electrolysis, 16.7 mA cm^{-2}, pH 6, 25℃).

Figure 5-5 explains the chlorine generation pathway on the blue TNA-RuO_2 compared with the blue TNA and RuO_2 examined by a $^{\bullet}OH$ probe compound (RNO) and $^{\bullet}OH$ scavenger (*t*-BuOH). As shown in Figure 5-5, $^{\bullet}OH$ generation was decreased on the blue TNA-RuO_2 compared with that of the blue TNA because part of the blue TNA is covered by RuO_2 while the $^{\bullet}OH$ generation on the RuO_2 is negligible. RNO degradation in log scale exhibited linearity with time following pseudo first-order kinetics, which implies the steady state $^{\bullet}OH$ generation.

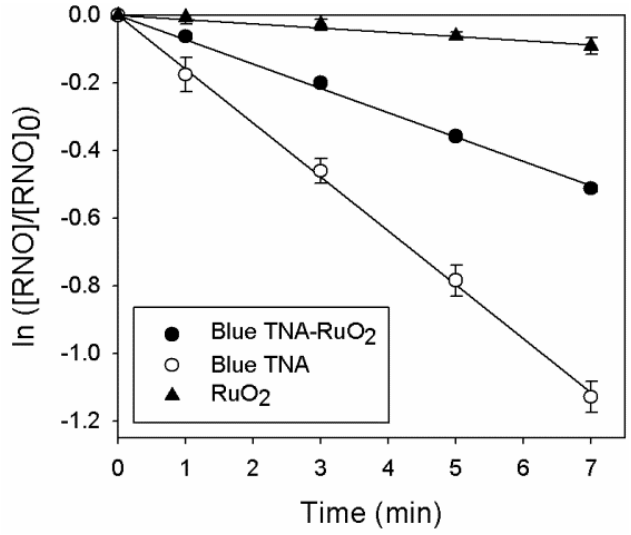

Figure 5-5. Chlorine generation pathway on the blue TNA-RuO_2 compared with the blue TNA and RuO_2 examined by RNO degradation ($^{\bullet}OH$ probe compound).

($[KH_2PO_4]_0$ = 0.1 M, $[RNO]_0 = 2 \times 10^{-5}$ M, 16.7 mA cm^{-2}, pH 7, 25℃).

Figure 5-6 shows the electrochemical activity of the electrodes measured with cyclic voltammetry from 0 V to 2.0 V (vs. Ag/AgCl) with a 50 mV s^{-1} scan rate. As shown in Figure 5-6, RuO_2 shows the highest electrochemical activity followed by the blue TNA-RuO_2. The chlorine generating current was not measured for the blue TNA in this potential region because of the high chlorine generating overpotential. Comparing the blue TNA-RuO_2 to the RuO_2 electrodes, the electrochemical activity is higher on the RuO_2 than that of blue TNA-RuO_2 while the chlorine generating current efficiency showed the reversed results. That could be explained with the chlorine generating selectivity. The RuO_2 is also known as oxygen generating electrode which is favored in the 0 to 2.0 V potential regions, the electrochemical activity for RuO_2 is combination of oxygen and chlorine generation. Other than the chlorine generating current efficiency of RuO_2 (82%) is seems to be oxygen generation (18%), while the oxygen generation is negligible for blue TNA-RuO_2, which showed 96% of chlorine generating current efficiency.

Moreover, the blue TNA-RuO_2 shows the same onset potential for chlorine generation as RuO_2 which means the coated RuO_2 participates as the electrocatalytic active site and contributes to the high chlorine generation performance.

Also, blue TNA showed higher capacitance than other electrodes while the capacitance of the blue TNA-RuO_2 was decreased compared to that of the blue TNA. The blue TNA is known to have a high capacitance because of the

nanotube structure; on the other hand, part of the pores was blocked on the blue TNA-RuO_2 causing the decrease in the capacitance. The capacitance properties explained by Figure 5-6 support the surface characterization of the blue TNA-RuO_2 in Figure 5-1(a).

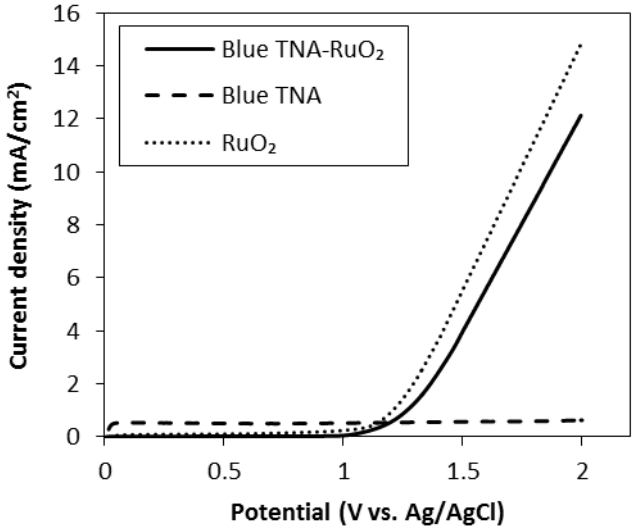

Figure 5-6. Electrochemical activity of the electrodes measured with cyclic voltammetry.

($[NaCl]_0$ = 0.1 M, pH 6, 25℃, 50 mV s^{-1}).

Figure 5-7 shows the direct and indirect pathways of chlorine generation on the blue TNA-RuO_2 electrode. The blue TNA-RuO_2 electrode consists of the blue TNA part and the RuO_2 part because the RuO_2 is coated onto the blue TNA (Figure 5-1(a)). RuO_2 and blue TNA have different pathways for chlorine generation. Chlorine is generated directly on RuO_2 by oxidation of the chloride ions while the $^{\bullet}OH$ is first generated by water splitting on the blue TNA. $^{\bullet}OH$ radicals are further reacted with chloride ions to generate chlorine (Figure 5-5). Because of the synergetic effect on the RuO_2 and blue TNA, the blue TNA-RuO_2 electrode has a high efficiency and low energy consumption for the chlorine generation (Figure 5-3(b)). The low energy consumption and high chlorine generation of the blue TNA-RuO_2 have advantages for the chlorine generation industry. Additionally, the chlorine generating pathway on the blue TNA can be modified by controlling the area of the blue TNA and the amount of RuO_2 coating for applications in various industrial fields where different types of oxidants are required.

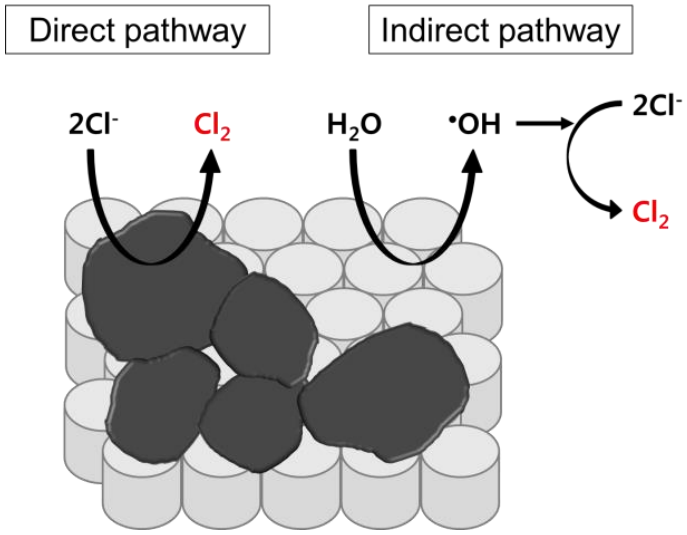

Figure 5-7. Direct and indirect pathways of chlorine generation on the blue TNA-RuO_2 electrode.

5.4. Summary

In this study, a novel blue TNA-RuO_2 electrode was fabricated by coating the RuO_2 onto the blue TNA (blue TNA-RuO_2) to increase the chlorine generation by utilizing the direct and indirect pathways simultaneously on one electrode. The blue TNA-RuO_2 had a higher current efficiency and lower energy consumption (96%, 3.2 Wh g^{-1}) than that of the blue TNA (74%, 6.2 Wh g^{-1}) and RuO_2 (82%, 3.3 Wh g^{-1}). It was well demonstrated that the RuO_2 component on the blue TNA-RuO_2 electrode contributed to direct chlorine generation, and the blue TNA component contributed to the indirect pathway of chlorine generation. This study suggests that blue TNA-RuO_2 as an efficient electrode for chlorine generation can be suitably applied to various industrial fields where chlorine is used.

6. Conclusion

In this study, the classification method for electrochemical oxidant generating electrodes was developed by using the •OH scavengers and it is applied for the investigation of the precursor for peroxodisulfate generation and for the development of highly efficient chlorine generating electrode.

Firstly, a novel quantitative classification method for oxidant generating electrodes was developed. Ten electrodes were classified into three types, active (A), inactive-surface adsorbed ($I_{\cdot OH,s}$), and inactive-free ($I_{\cdot OH,f}$). More specifically, RuO_2, IrO_2, Pt, Bi-TiO_2/Ta-IrO_2, and RuO_2-IrO_2 were classified as {A}, Ni-Sb-SnO_2 and Sb-SnO_2 were classified as {$I_{\cdot OH,s}$ & $I_{\cdot OH,f}$}, and Black TNA, Blue TNA and BDD were classified as {$I_{\cdot OH,f}$}. Also, those electrodes were quantitatively expressed, for the better understanding of oxidants generating properties of electrodes, according to the oxidants generating pathways as {R_A, $R_{\cdot OH,s}$, $R_{\cdot OH,f}$} such as RuO_2{0.93, 0.07, 0} and blue TNA{0.04, 0.17, 0.79}.

Secondly, the types of •OH (surface adsorbed or free) as a key precursor for PDS generation were figured out by comparing the electrode classification and PDS generation on six •OH generating electrodes. PDS generation showed linear relationship with Cl_2,$_{\cdot OH,f}$ which means that the free •OH is the key precursor for PDS generation. Also, self-doped TNAs (blue TNA and black TNA) were reported for superior PDS generating properties with cost-

effective material, which was comparable with that of BDD, well-known PDS generating electrode. The PDS generating efficiency on blue TNA, black TNA and BDD were 46%, 41%, and 22%, respectively. High PDS generating efficiency on blue TNA was because of the free $^{\bullet}OH$ generation on blue TNA.

Thirdly, RuO_2 coated blue TNA was developed to improve the chlorine generation of blue TNA. Blue TNA-RuO_2 (96%, 3.2 Wh g^{-1}) showed the higher chlorine generation efficiency than that of blue TNA (74%) and RuO_2 (82%), while the energy consumption was comparable to RuO_2 (3.3 Wh g^{-1}), which is much lower than that of blue TNA (6.2 Wh g^{-1}). High performance on blue TNA-RuO_2 was due to the synergetic effect of direct and indirect pathways for chlorine generation.

The results of this study can improve the understanding of mechanisms for oxidants generation, especially with the novel classification method, and contribute to the development of electrodes for $^{\bullet}OH$ involving oxidants generation.

References

Association, A. P. H., A. W. W. Association and W. E. Federation (2005). Standard methods for the examination of water and wastewater. *American Public Health Association (APHA)*.

Augustynski, J., L. Balsenc and J. Hinden (1978). X-Ray Photoelectron Spectroscopic Studies of RuO_2-Based Film Electrodes. *Journal of the Electrochemical Society* **125**(7): 1093-1097.

Bard, A. J. and L. R. Faulkner (2001). *Electrochemical Methods: Fundamentals and Applications*. New York, Wiley.

Bertsch-Frank, B., D. Engel, P. Kleinschmit, T. Lehmann, P. Panster, N. Steiner and S. Jacobi (2011). Peroxo compounds, inorganic. *Ullmann's Encyclopedia of Industrial Chemistry*.

Burke, L. D. and J. F. O'Neill (1979). Some aspects of the chlorine evolution reaction at ruthenium dioxide anodes. *Journal of Electroanalytical Chemistry and Interfacial Electrochemistry* **101**(3): 341-349.

Buxton, G. V., C. L. Greenstock, W. P. Helman and A. B. Ross (1988). Critical review of rate constants for reactions of hydrated electrons, hydrogen atoms and hydroxyl radicals (· OH/· O− in aqueous solution. *Journal of Physical and Chemical Reference Data* **17**(2): 513-886.

Cañizares, P., J. García-Gómez, J. Lobato and M. A. Rodrigo (2004). Modeling of wastewater electro-oxidation processes part I. General

description and application to inactive electrodes. *Industrial and Engineering Chemistry Research* **43**(9): 1915-1922.

Cañizares, P., C. Sáez, A. Sánchez-Carretero and M. Rodrigo (2009). Synthesis of novel oxidants by electrochemical technology. *Journal of Applied Electrochemistry* **39**(11): 2143.

Cao, H., D. Lu, J. Lin, Q. Ye, J. Wu and G. Zheng (2013). Novel Sb-doped ruthenium oxide electrode with ordered nanotube structure and its electrocatalytic activity toward chlorine evolution. *Electrochimica Acta* **91**: 234-239.

Chen, R., V. Trieu, A. R. Zeradjanin, H. Natter, D. Teschner, J. Kintrup, A. Bulan, W. Schuhmann and R. Hempelmann (2012). Microstructural impact of anodic coatings on the electrochemical chlorine evolution reaction. *Physical Chemistry Chemical Physics* **14**(20): 7392-7399.

Cho, K. and M. R. Hoffmann (2015). $Bi_xTi_{1-x}O_z$ functionalized heterojunction anode with an enhanced reactive chlorine generation efficiency in dilute aqueous solutions. *Chemistry of Materials* **27**(6): 2224-2233.

Cho, M., H. Chung, W. Choi and J. Yoon (2005). Different inactivation behaviors of MS-2 phage and Escherichia coli in TiO_2 photocatalytic disinfection. *Applied and Environmental Microbiology* **71**(1): 270-275.

Choi, J., C. G. Park and J. Yoon (2013). Application of an electrochemical chlorine-generation system combined with solar energy as appropriate

technology for water disinfection. *Transactions of the Royal Society of Tropical Medicine and Hygiene* **107**(2): 124-128.

Choi, J., S. Shim and J. Yoon (2013). Design and operating parameters affecting an electrochlorination system. *Journal of Industrial and Engineering Chemistry* **19**(1): 215-219.

Clifton, C. L. and R. E. Huie (1989). Rate constants for hydrogen abstraction reactions of the sulfate radical, SO4−. Alcohols. *International Journal of Chemical Kinetics* **21**(8): 677-687.

Comninellis, C. (1994). Electrocatalysis in the electrochemical conversion/combustion of organic pollutants for waste water treatment. *Electrochimica Acta* **39**(11): 1857-1862.

Comninellis, C., A. Kapalka, S. Malato, S. A. Parsons, I. Poulios and D. Mantzavinos (2008). Advanced oxidation processes for water treatment: advances and trends for R&D. *Journal of Chemical Technology and Biotechnology* **83**(6): 769-776.

Conway, B. and M. Salomon (1964). Electrochemical reaction orders: Applications to the hydrogen-and oxygen-evolution reactions. *Electrochimica Acta* **9**(12): 1599-1615.

Cordfunke, E. and R. Konings (1988). The enthalpy of formation of RuO< sub> 2</sub>. *Thermochimica Acta* **129**(1): 63-69.

Davis, J., J. C. Baygents and J. Farrell (2014). Understanding persulfate production at boron doped diamond film anodes. *Electrochimica Acta* **150**: 68-74.

Davis, J. R., J. C. Baygents and J. Farrell (2014). Effect of current density and sulfuric acid concentration on persulfuric acid generation by boron-doped diamond film anodes. *Journal of Applied Electrochemistry* **44**(7): 841-848.

Delahay, P. and P. Ruetschi (1954). INFLUENCE OF ELECTRODE MATERIAL ON OXYGEN OVERVOLTAGE-A THEORETICAL ANALYSIS, Louisiana State University Baton Rouge.

El-Morsi, T. M., W. R. Budakowski, A. S. Abd-El-Aziz and K. J. Friesen (2000). Photocatalytic degradation of 1, 10-dichlorodecane in aqueous suspensions of TiO_2: a reaction of adsorbed chlorinated alkane with surface hydroxyl radicals. *Environmental Science and Technology* **34**(6): 1018-1022.

Elovitz, M. S. and U. von Gunten (1999). Hydroxyl radical/ozone ratios during ozonation processes. I. The R_{ct} concept. *Ozone Science and Engineering* **21**(3): 239-260.

Erenburg, R., L. Krishtalik and V. Bystrov (1972). Mechanism of chlorine evolution and ionization on a ruthenium oxide electrode. *Elektrokhirniya* **8**: 1740.

Erenburg, R., L. Krishtalik and I. Yaroshevskaya (1975). Mechanism of chlorine evolution at a ruthenium-titanium oxide electrode. *Soviet Electrochemistry* **11**(7): 989-992.

Faita, G. and G. Fiori (1972). Anodic discharge of chloride ions on oxide electrodes. *Journal of Applied Electrochemistry* **2**(1): 31-35.

Farhat, A., J. Keller, S. Tait and J. Radjenovic (2015). Removal of persistent organic contaminants by electrochemically activated sulfate. *Environmental Science & Technology* **49**(24): 14326-14333.

Fernández, J., M. Gennero de Chialvo and A. Chialvo (2002). Kinetic study of the chlorine electrode reaction on Ti/RuO_2 through the polarisation resistance: Part III: proposal of a reaction mechanism. *Electrochimica Acta* **47**(7): 1145-1152.

Ferro, S. and A. De Battisti (2002). Electrocatalysis and chlorine evolution reaction at ruthenium dioxide deposited on conductive diamond. *The Journal of Physical Chemistry B* **106**(9): 2249-2254.

Guerrini, E., V. Consonni and S. Trasatti (2005). Surface and electrocatalytic properties of well-defined and vicinal RuO_2 single crystal faces. *Journal of Solid State Electrochemistry* **9**(5): 320-329.

Hansen, H. A., I. C. Man, F. Studt, F. Abild-Pedersen, T. Bligaard and J. Rossmeisl (2010). Electrochemical chlorine evolution at rutile oxide (110) surfaces. *Physical Chemistry Chemical Physics* **12**(1): 283-290.

Hepel, T., F. H. Pollak and W. E. O'Grady (1986). Chlorine Evolution and Reduction Processes at Oriented Single-Crystal RuO2 Electrodes. *Journal of the Electrochemical Society* **133**(1): 69-75.

Iniesta, J., P. Michaud, M. Panizza, G. Cerisola, A. Aldaz and C. Comninellis (2001). Electrochemical oxidation of phenol at boron-doped diamond electrode. *Electrochimica Acta* **46**(23): 3573-3578.

J. O'M, B. (1956). Kinetics of Activation Controlled Consecutive Electrochemical Reactions: Anodic Evolution of Oxygen. *Journal of Chemical Physics* **24**: 817-827.

Janssen, L., G. Visser and E. Barendrecht (1983). Effect of molecular chlorine diffusion on theoretical potential-current density relations for chlorine evolving electrode. *Electrochimica Acta* **28**(2): 155-163.

Jeong, J., C. Kim and J. Yoon (2009). The effect of electrode material on the generation of oxidants and microbial inactivation in the electrochemical disinfection processes. *Water Research* **43**(4): 895-901.

Jirkovský, J., H. Hoffmannová, M. Klementová and P. Krtil (2006). Particle size dependence of the electrocatalytic activity of nanocrystalline RuO_2 electrodes. *Journal of the Electrochemical Society* **153**(6): E111-E118.

Kapałka, A., G. Fóti and C. Comninellis (2008). Determination of the Tafel slope for oxygen evolution on boron-doped diamond electrodes. *Electrochemistry Communications* **10**(4): 607-610.

Khamis, D., E. Mahé, F. Dardoize and D. Devilliers (2010). Peroxodisulfate generation on boron-doped diamond microelectrodes array and detection by scanning electrochemical microscopy. *Journal of Applied Electrochemistry* **40**(10): 1829-1838.

Kim, C., S. Kim, J. Choi, J. Lee, J. S. Kang, Y.-E. Sung, J. Lee, W. Choi and J. Yoon (2014). Blue TiO_2 nanotube array as an oxidant generating novel anode material fabricated by simple cathodic polarization. *Electrochimica Acta* **141**: 113-119.

Kim, C., S. Kim, S. P. Hong, J. Lee and J. Yoon (2016). Effect of doping level of colored TiO2 nanotube arrays fabricated by electrochemical self-doping on electrochemical properties. *Physical Chemistry Chemical Physics* **18**(21): 14370-14375.

Kim, C., S. Kim, S. P. Hong, J. Lee and J. Yoon (2016). Effect of doping level of colored TiO 2 nanotube arrays fabricated by electrochemical self-doping on electrochemical properties. *Physical Chemistry Chemical Physics* **18**(21): 14370-14375.

Kim, C., S. Kim, J. Lee, J. Kim and J. Yoon (2015). Capacitive and oxidant generating properties of Black-colored TiO_2 nanotube array fabricated by electrochemical self-doping. *ACS Applied Materials and Interfaces* **7**(14): 7486-7491.

Kim, C., S. Lee, S. Kim and J. Yoon (2016). Effect of Annealing Temperature on the Capacitive and Oxidant-generating Properties of an

Electrochemically Reduced TiO 2 Nanotube Array. *Electrochimica Acta* **222**: 1578-1584.

Kim, C., H.-j. Park, S. Cha and J. Yoon (2013). Facile detection of photogenerated reactive oxygen species in TiO 2 nanoparticles suspension using colorimetric probe-assisted spectrometric method. *Chemosphere* **93**(9): 2011-2015.

Kim, J., C. Kim, S. Kim and J. Yoon (2015). A review of chlorine evolution mechanism on Dimensionally Stable Anode (DSA®). *Korean Chemical Engineering Research* **53**(5): 531-539.

Kim, K.-W., E.-H. Lee, J.-S. Kim, K.-H. Shin and K.-H. Kim (2001). Study on the electro-activity and non-stochiometry of a Ru-based mixed oxide electrode. *Electrochimica Acta* **46**(6): 915-921.

Kim, M. S., K.-M. Lee, H.-E. Kim, H.-J. Lee, C. Lee and C. Lee (2016). Disintegration of waste activated sludge by thermally-activated persulfates for enhanced dewaterability. *Environmental Science & Technology* **50**(13): 7106-7115.

Kim, S. and W. Choi (2002). Kinetics and mechanisms of photocatalytic degradation of $(CH_3)_nNH_{4-n}^+$ ($0 \leq n \leq 4$) in TiO_2 suspension: The role of OH radicals. *Environmental Science and Technology* **36**(9): 2019-2025.

Kolthoff, I. and I. Miller (1951). The chemistry of persulfate. I. The kinetics and mechanism of the decomposition of the persulfate ion in aqueous medium1. *Journal of the American Chemical Society* **73**(7): 3055-3059.

Krishtalik, L. (1981). Kinetics and mechanism of anodic chlorine and oxygen evolution reactions on transition metal oxide electrodes. *Electrochimica Acta* **26**(3): 329-337.

Le Luu, T., J. Kim and J. Yoon (2014). Physicochemical properties of RuO_2 and IrO_2 electrodes affecting chlorine evolutions. *Journal of Industrial and Engineering Chemistry*.

Lee, H., H.-J. Lee, J. Jeong, J. Lee, N.-B. Park and C. Lee (2015). Activation of persulfates by carbon nanotubes: oxidation of organic compounds by nonradical mechanism. *Chemical Engineering Journal* **266**: 28-33.

Liang, C., C.-F. Huang, N. Mohanty and R. M. Kurakalva (2008). A rapid spectrophotometric determination of persulfate anion in ISCO. *Chemosphere* **73**(9): 1540-1543.

Liu, H., T. A. Bruton, W. Li, J. V. Buren, C. Prasse, F. M. Doyle and D. L. Sedlak (2016). Oxidation of benzene by persulfate in the presence of Fe (III)-and Mn (IV)-containing oxides: stoichiometric efficiency and transformation products. *Environmental Science & Technology* **50**(2): 890-898.

Lodi, G., E. Sivieri, A. De Battisti and S. Trasatti (1978). Ruthenium dioxide-based film electrodes. *Journal of Applied Electrochemistry* **8**(2): 135-143.

Losev, V., N. Y. Bune and L. Chuvaeva (1989). Specific features of the kinetics of gas-evolving reactions on highly active electrodes. *Electrochimica Acta* **34**(7): 929-942.

Lu, Z., C. T. Yip, L. Wang, H. Huang and L. Zhou (2012). Hydrogenated TiO2 Nanotube Arrays as High-Rate Anodes for Lithium-Ion Microbatteries. *ChemPlusChem* **77**(11): 991-1000.

Luu, T. L., C. Kim, J. Kim, S. Kim and J. Yoon (2015). The Effect of Preparation Parameters in Thermal Decomposition of Ruthenium Dioxide Electrodes on Chlorine Electro-Catalytic Activity. *Bulletin of the Korean Chemical Society* **36**(5): 1411-1417.

Marselli, B., J. Garcia-Gomez, P.-A. Michaud, M. Rodrigo and C. Comninellis (2003). Electrogeneration of hydroxyl radicals on boron-doped diamond electrodes. *Journal of the Electrochemical Society* **150**(3): D79-D83.

Michaud, P. A., E. Mahé, W. Haenni, A. Perret and C. Comninellis (2000). Preparation of Peroxodisulfuric Acid Using Boron-Doped Diamond Thin Film Electrodes. *Electrochemical and Solid-State Letters* **3**(2): 77-79.

Neta, P., R. E. Huie and A. B. Ross (1988). Rate constants for reactions of inorganic radicals in aqueous solution. *Journal of Physical and Chemical Reference Data* **17**(3): 1027-1284.

Over, H. (2013). Atomic scale insights into electrochemical versus gas phase oxidation of HCl over RuO_2-based catalysts: A comparative review. *Electrochimica Acta* **93**: 313-333.

Palme, H. (1920). Studien über die Zersetzung der Ü berschwefelsäure. *Zeitschrift fur Anorganische und Allgemeine Chemie* **112**(1): 97-130.

Panizza, M. and G. Cerisola (2005). Application of diamond electrodes to electrochemical processes. *Electrochimica Acta* **51**(2): 191-199.

Pankratiev, Y. D. (1982). Correlation between oxygen binding energy and catalytic activity of oxides. *Reaction Kinetics and Catalysis Letters* **20**(3-4): 255-259.

Rueffer, M., D. Bejan and N. J. Bunce (2011). Graphite: An active or an inactive anode? *Electrochimica Acta* **56**(5): 2246-2253.

Serrano, K., P. Michaud, C. Comninellis and A. Savall (2002). Electrochemical preparation of peroxodisulfuric acid using boron doped diamond thin film electrodes. *Electrochimica Acta* **48**(4): 431-436.

Simonsen, M. E., J. Muff, L. R. Bennedsen, K. P. Kowalski and E. G. Søgaard (2010). Photocatalytic bleaching of p-nitrosodimethylaniline and a comparison to the performance of other AOP technologies. *Journal of Photochemistry and Photobiology A: Chemistry* **216**(2): 244-249.

Sirés, I., E. Brillas, M. A. Oturan, M. A. Rodrigo and M. Panizza (2014). Electrochemical advanced oxidation processes: today and tomorrow. A review. *Environmental Science and Pollution Research* **21**(14): 8336-8367.

Smit, W. and J. Hoogland (1971). The mechanism of the anodic formation of the peroxodisulphate ion on platinum—I. establishment of the participating anion. *Electrochimica Acta* **16**(1): 1-18.

Stafford, U., K. A. Gray and P. V. Kamat (1994). Radiolytic and TiO2-assisted photocatalytic degradation of 4-chlorophenol. A comparative study. *The Journal of Physical Chemistry* **98**(25): 6343-6351.

Sun, Y. and J. J. Pignatello (1995). Evidence for a surface dual hole-radical mechanism in the titanium dioxide photocatalytic oxidation of 2, 4-D. *Environmental Science & Technology* **29**(8): 2065-2072.

Thomassen, M., C. Karlsen, B. Børresen and R. Tunold (2006). Kinetic investigation of the chlorine reduction reaction on electrochemically oxidised ruthenium. *Electrochimica Acta* **51**(14): 2909-2918.

Trasatti, S. (1984). Electrocatalysis in the anodic evolution of oxygen and chlorine. *Electrochimica Acta* **29**(11): 1503-1512.

Trasatti, S. (1987). Progress in the understanding of the mechanism of chlorine evolution at oxide electrodes. *Electrochimica Acta* **32**(3): 369-382.

Trasatti, S. (2000). Electrocatalysis: understanding the success of DSA®. *Electrochimica Acta* **45**(15): 2377-2385.

Trieu, V., B. Schley, H. Natter, J. Kintrup, A. Bulan and R. Hempelmann (2012). RuO< sub> 2</sub>-based anodes with tailored surface morphology for improved chlorine electro-activity. *Electrochimica Acta* **78**: 188-194.

Wardman, P. (1989). Reduction potentials of one-electron couples involving free radicals in aqueous solution. *Journal of Physical and Chemical Reference Data* **18**(4): 1637-1755.

Yang, S. Y., D. Kim and H. Park (2014). Shift of the Reactive Species in the Sb–SnO2-Electrocatalyzed Inactivation of E. coli and Degradation of Phenol: Effects of Nickel Doping and Electrolytes. *Environmental Science & Technology* **48**(5): 2877-2884.

Zeradjanin, A. R., N. Menzel, P. Strasser and W. Schuhmann (2012). Role of Water in the Chlorine Evolution Reaction at RuO2-Based Electrodes—Understanding Electrocatalysis as a Resonance Phenomenon. *ChemSusChem* **5**(10): 1897-1904.

Zhu, X., M. Tong, S. Shi, H. Zhao and J. Ni (2008). Essential explanation of the strong mineralization performance of boron-doped diamond electrodes. *Environmental Science & Technology* **42**(13): 4914-4920.

국문초록

전기화학적 산화제 생성 공정은 고도산화공정, 하수처리, 클로로알칼리 공정, 고분자 합성 등에서 널리 사용된다. 전기화학적 산화제 생성 공정에서는 전극 물질 및 전기분해 조건에 따라 염소 (Cl_2), 수산화라디칼 ($^{\bullet}OH$), 과황산 (peroxodisulfate; PDS), 오존 (O_3), 과산화수소 (H_2O_2) 등 다양한 산화제가 생성될 수 있다. 널리 사용되는 전극 물질로는 치수안정성 전극 (Dimensionally stable anode; DSA®), 보론 도핑 다이아몬드 전극 (boron doped diamond; BDD), Sb-SnO_2 등이 있으며, 최근 self-doped TiO_2 나노튜브 (blue and black TiO_2 나노튜브) 와 Bi-TiO_2/Ta-IrO_2 또한 보고되었다. 산화제 생성 경로에 따라 전극은 active 전극과 inactive 전극으로 구분된다. 그러나, 이러한 분류 방법은 전극에서 생성되는 표면 흡착 수산화 라디칼과 자유 라디칼을 구분하기 어려우며, 최근 개발된 전극들이 분류되어 있지 않다는 한계점이 있다. 또한, PDS 와 같이 수산화 라디칼이 관여하는 산화제 생성 과정에서 관여하는 수산화라디칼의 종류가 구분되어 있지 않아 효과적인 전극 사용 및 새로운 전극 개발에 한계가 있다. 따라서, 흡착 수산화라디칼과 자유 라디칼을 구분한

전극 분류 방법 제시 및 산화제 생성 시 관여하는 수산화라디칼의 종류 규명, 서로 다른 산화제 생성 경로를 활용한 고효율 전극의 개발이 필요한 실정이다.

본 연구의 목적은 새로운 전극 분류 방법을 개발하고, PDS 생성 메커니즘 연구 및 새로운 염소 발생 전극 개발에 활용하는 것이다. 주요 결과로, 먼저, 산화제 생성 전극을 위한 정량적 전극 분류 방법을 개발하였다. 표면 흡착 수산화라디칼과 자유 라디칼을 서로 다르게 소거하는 수산화라디칼 소거제 (*t*-부탄올과 메탄올)을 사용하여 9 개의 전극이 active (A), inactive-surface adsorbed ($I_{OH,s}$), and inactive-free ($I_{OH,f}$) 의 세 가지로 분류되었으며, 전극 물질을 산화제 생성 경로에 따라 {R_A, $R_{OH,s}$, $R_{OH,f}$}, 즉, RuO_2{0.93, 0.07, 0}, blue TNA{0.04, 0.17, 0.79} 와 같이 정량적으로 확인하였다.

두번째로, PDS 생성의 주요 전구체를 규명하였다. PDS 생성이 자유 라디칼 농도와 선형적 관계를 보였으며, 이를 통해 자유 라디칼이 PDS 생성의 전구체임을 알 수 있다. 전체 수산화라디칼 농도 혹은 표면 흡착 수산화라디칼은 PDS 생성과 연관성을 보이지 않았다. 또한, PDS 생성 성능이 뛰어난 전극으로 blue TNA 를 보고하였다. Blue TNA 는 기존 PDS 생성 전극으로 알려진 BDD 에 비해 저렴하고 제조가 용이한 물질로, BDD 와 유사한 PDS 생성 성능을

나타내었다. Blue TNA 와 BDD 의 PDS 생성 전류 효율은 각각 46% 와 41% 로 나타났다. Blue TNA 에서의 높은 PDS 생성 성능은 blue TNA 에서 생성되는 자유 라디칼에 의한 것임을 확인하였다.

세번째로, 염소 발생 전극으로 RuO_2 코팅된 blue TNA 전극을 개발하였다. blue TNA-RuO_2 (96%) 는 blue TNA (74%) 혹은 RuO_2 (82%) 에 비해 높은 염소 생성 전류 효율을 보였으며, blue TNA-RuO_2 의 에너지 소모량 (3.2 Wh g^{-1}) 은 RuO_2 (3.3 Wh g^{-1}) 와 유사하고, blue TNA (6.2 Wh g^{-1}) 에 비해 절반 정도의 에너지를 소모함을 확인하였다. blue TNA-RuO_2 에서의 고성능 염소 발생은 직접 염소 발생과 수산화라디칼에 의한 간접 염소 발생의 시너지 효과에 의한 것임을 확인하였다.

본 연구에서의 결과들은 세부적인 전극 분류를 통해 산화제 생성 경로에 대한 이해와, 이후 고성능 산화제 생성 전극의 개발에 기여할 것으로 생각된다.

주요어: 전극 분류, 전기화학적 산화제 생성, 표면 흡착 수산화라디칼, 자유 라디칼, 수산화라디칼 소거, 염소 생성, 과황산 생성, blue TiO_2 나노 튜브 전극

학 번: 2012-23976